Al incorporation up to 99% in MOCVD grown monoclinic $(Al_xGa_{1-x})_2O_3$ films using trimethylgallium

A F M Anhar Uddin Bhuiyan[1, a)], Lingyu Meng[1], Hsien-Lien Huang[2], Christopher Chae[2], Jinwoo Hwang[2], and Hongping Zhao[1, 2, b)]

[1]*Department of Electrical and Computer Engineering, The Ohio State University, Columbus, OH 43210, USA*
[2]*Department of Materials Science and Engineering, The Ohio State University, Columbus, OH 43210, USA*
[a)] Email: bhuiyan.13@osu.edu
[b)] Corresponding author Email: zhao.2592@osu.edu

Abstract

Growths of monoclinic $(Al_xGa_{1-x})_2O_3$ thin films up to 99% Al contents are demonstrated via metalorganic chemical vapor deposition (MOCVD) using trimethylgallium (TMGa) as the Ga precursor. The utilization of TMGa, rather than triethylgallium (TEGa), enables a significant improvement of the growth rates (> 2.5 μm/hr) of β-$(Al_xGa_{1-x})_2O_3$ thin films on (010), (100) and $(\bar{2}01)$ β-Ga_2O_3 substrates. By systematically tuning the precursor molar flow rates, growth of coherently strained phase pure β-$(Al_xGa_{1-x})_2O_3$ films are demonstrated by comprehensive material characterizations via high-resolution x-ray diffraction (XRD) and atomic resolution scanning transmission electron microscopy (STEM) imaging. Monoclinic $(Al_xGa_{1-x})_2O_3$ films with Al contents up to 99%, 29% and 16% are achieved on (100), (010) and $(\bar{2}01)$ β-Ga_2O_3 substrates, respectively. Beyond 29% of Al incorporation, the (010) $(Al_xGa_{1-x})_2O_3$ films exhibit β- to γ-phase segregation. β-$(Al_xGa_{1-x})_2O_3$ films grown on $(\bar{2}01)$ β-Ga_2O_3 show local segregation of Al along (100) plane. Record-high Al incorporations up to 99% in monoclinic $(Al_xGa_{1-x})_2O_3$ grown on (100) Ga_2O_3 is confirmed from XRD, STEM, electron nano-diffraction and x-ray photoelectron spectroscopy (XPS) measurements. These results indicate great promises of MOCVD

development of β-$(Al_xGa_{1-x})_2O_3$ films and heterostructures with high Al content and growth rates using TMGa for next generation high power and high frequency electronic devices.

Keywords: Ultrawide bandgap, β-$(Al_xGa_{1-x})_2O_3$ alloy, β-Ga_2O_3 substrates, metalorganic chemical vapor deposition (MOCVD), bandgap engineering

I. Introduction

Monoclinic gallium oxide (β-Ga_2O_3) has received a lot of attention over the past decade as a potential new material platform for power electronics. Due to its promising properties, such as its ultrawide bandgap (UWBG) energy (~ 4.87 eV) [1], high predicted breakdown field strength (~ 8 MV/cm) [2] and controllable n-type doping capability [3-5], β-Ga_2O_3 has been considered as a viable candidate for the development of high-power electronics and ultraviolet optoelectronics with capabilities beyond existing technologies based on the traditional wide bandgap (WBG) GaN and SiC. In addition, producing high-quality, large diameter, and uniform β-Ga_2O_3 bulk crystals through melt growth techniques is scalable and predicted to be low cost as compared to vapor growth techniques for GaN and SiC bulk substrates [6-9]. Furthermore, β-Ga_2O_3 substrates are available with different crystal planes, including (010), (100), (001) and $(\bar{2}01)$, allowing for homoepitaxial growth along different orientations with engineered structural, electrical, and optical properties. Another promising advantage of β-Ga_2O_3 is its ability of bandgap engineering by alloying with Al_2O_3, which tunes its bandgap from 4.87 to 8.82 eV with a predicted breakdown field strength up to 16 MV/cm of $(Al_xGa_{1-x})_2O_3$ ($x < 80\%$) [1, 10]. The efforts on developing high-quality epitaxy of β-$(Al_xGa_{1-x})_2O_3$ with a wide range of Al content, controllable doping [11-19], and β-$(Al_xGa_{1-x})_2O_3/Ga_2O_3$ heterostructures have led to the demonstrations of high-performance

modulation-doped field-effect transistors (MODFETs) [20-22], which are promising for the next-generation high-power and high-frequency electronic applications.

In order to develop vertical high-power devices with high breakdown field strength and maximize the mobility and carrier density in β-$(Al_xGa_{1-x})_2O_3$/Ga_2O_3 based lateral devices [10, 23, 24], it is critical to achieve high quality β-$(Al_xGa_{1-x})_2O_3$ films with higher Al contents [25]. Molecular beam epitaxy (MBE) [26, 27] and MOCVD [11-13, 15, 16, 28-34] are commonly used techniques for epitaxial growth of β-$(Al_xGa_{1-x})_2O_3$ thin films. While MBE growth of (010) β-$(Al_xGa_{1-x})_2O_3$ films are demonstrated with sharp interfaces and good homogeneity, the growth rates (~ 0.19 μm/hr) and Al contents (< 20%) are still limited [26]. In contrast, phase pure (010) β-$(Al_xGa_{1-x})_2O_3$ films are reported with Al contents of < 35% with relatively higher growth rates (~ 0.6-0.96 μm/hr) by MOCVD [11, 12, 35]. However, targeting for higher Al contents results in phase segregation in (010) β-$(Al_xGa_{1-x})_2O_3$ films [12], regardless of the growth methods. Although it is important to develop high quality β-$(Al_xGa_{1-x})_2O_3$ films with high Al contents, the different ground state crystal structures of two parent materials [1]: monoclinic β-Ga_2O_3 (space group C2/m) and corundum α-Al_2O_3 (space group $R\bar{3}c$) make it challenging to maximize the Al contents. While the incorporation of higher Al contents in β-$(Al_xGa_{1-x})_2O_3$ films on (010) β-Ga_2O_3 substrates is found to be difficult due to the coexistence of different phases (β and γ) [12], the use of other planes of β-Ga_2O_3 substrates such as (100) [15] and $(\bar{2}01)$ [16] leads to more than 50% Al incorporation in single crystal β-$(Al_xGa_{1-x})_2O_3$ films, indicating strong influence of crystal orientations on the solubility limit of Al in β-$(Al_xGa_{1-x})_2O_3$ films.

Calculations based on density functional theory (DFT) [1] and equilibrium phase diagram [36] suggest the maximum Al contents of 71% and 67% in β-phase $(Al_xGa_{1-x})_2O_3$ films, respectively. Nevertheless, the experimental demonstrations of MOCVD growth of β-phase $(Al_xGa_{1-x})_2O_3$ films

are still limited up to 52%, 48%, 35% and 25% of Al contents along (100) [15] ($\bar{2}$01) [16], (010) [12, 35] and (001) [19] planes, respectively. In addition to the variation in Al incorporation along different planes, both experimental [35, 37] and theoretical calculations [38] of the band offsets at β-$(Al_xGa_{1-x})_2O_3$/Ga_2O_3 heterointerfaces also showed strong orientation and Al content dependency. In these prior investigations of MOCVD epitaxial growth of β-$(Al_xGa_{1-x})_2O_3$ films, triethylgallium (TEGa) was used as the Ga precursor, limiting growth rates below 1.0-0.7 μm/hr. On the other hand, both TEGa and TMGa have been used as Ga precursors for MOCVD homoepitaxial growth of β-Ga_2O_3 films. Due to its two-step decomposition process, TMGa enables higher growth rates of Ga_2O_3 films compared to TEGa, which undergoes a three-step pyrolysis process [39]. When TEGa is utilized as the Ga precursor in MOCVD β-Ga_2O_3 growth, the typical growth rates range from 0.2 to 1.0 μm/hr. In contrast, using TMGa as the Ga precursor has demonstrated faster growth rates of up to 3 μm/hr, while maintaining excellent transport characteristics similar to those grown using TEGa [5]. While our prior studies on MOCVD β-$(Al_xGa_{1-x})_2O_3$ epitaxy using TEGa as Ga precursor have revealed a strong impact of substrate orientation on the phase stabilization, solubility limit, band offset, critical thickness and n-type doping of β-$(Al_xGa_{1-x})_2O_3$ thin films, the use of TMGa as Ga precursor for epitaxial growth of β-$(Al_xGa_{1-x})_2O_3$ films has not yet been investigated.

In this work, for the first time, MOCVD growth of β-$(Al_xGa_{1-x})_2O_3$ films and β-$(Al_xGa_{1-x})_2O_3$/Ga_2O_3 superlattice (SL) structures are investigated on (010), (100) and ($\bar{2}$01) crystal planes using TMGa as Ga precursor to evaluate the influence of different orientations of the substrate on the solubility limit of β-$(Al_xGa_{1-x})_2O_3$ films grown with relatively fast growth rates. Owing to its higher vapor pressure and faster reaction kinetics of TMGa as compared to that of TEGa, our systematic growth studies of $(Al_xGa_{1-x})_2O_3$ films using TMGa show faster growth rates up to 2.53 μm/hr along different crystal orientations with record high Al incorporation up to 99% in

monoclinic $(Al_xGa_{1-x})_2O_3$ films without observing phase transformation. The crystalline structure, quality, strain, chemical content and surface morphology of β-$(Al_xGa_{1-x})_2O_3$ films and β-$(Al_xGa_{1-x})_2O_3/Ga_2O_3$ SLs grown with fast growth rates are investigated by comprehensive material characterizations, including XRD, high resolution STEM, STEM energy dispersive x-ray spectroscopy (EDX) mapping, XPS, atomic force microscopy (AFM) and field emission scanning electron microscopy (FESEM).

II. Experimental Details

The β-$(Al_xGa_{1-x})_2O_3$ thin films were grown on (010), (100) and $(\bar{2}01)$ oriented semi-insulating β-Ga_2O_3 substrates (purchased from Novel Crystal Technology) using Agnitron Agilis MOCVD reactor. Trimethylaluminum (TMAl) and TMGa were used as the Al and Ga precursors, respectively. Pure O_2 and Argon (Ar) were used as O-precursor and carrier gas, respectively. The growth temperature and the chamber pressure were set at 950 °C and 60 Torr, respectively. The TMGa molar flow rate was varied between 33.83 and 48.33 μmol min^{-1} and the TMAl molar flow rate was tuned from 1.5 to 11.59 μmol min^{-1}. The O_2 molar flow rate was set at 500 sccm. Prior to epitaxial growth initiation, ex-situ solvent cleaning was performed using acetone, isopropanol (IPA) and DI water.

The Al content, crystalline structure and strain of the films were characterized by XRD measurements using a Bruker D8 Discover with Cu Kα radiation x-ray source (λ =1.5418 Å). The surface morphology and surface roughness were evaluated using FESEM (FEI Helios 600) and AFM (Bruker AXS Dimension Icon), respectively. An aberration-corrected Thermo Fisher Scientific Themis-Z scanning transmission electron microscopy was used to obtain high angle annular dark field (HAADF) STEM images and EDX spectral mapping. Film thicknesses were determined using STEM-EDX elemental mapping profiles, high resolution STEM-HAADF

images of β-$(Al_xGa_{1-x})_2O_3$ thin films and cross-sectional FESEM images of $(Al_xGa_{1-x})_2O_3$ films grown on coloaded sapphire substrates. XPS measurements were performed by using Kratos Axis Ultra X-ray photoelectron spectrometer with a monochromatized Al Kα x-ray source (E_{photon} = 1486.6 eV) to confirm the Al contents and determine the bandgaps of β-$(Al_xGa_{1-x})_2O_3$ films with different Al contents.

III. Results and Discussions

The crystalline structure and the strain characteristics of β-$(Al_xGa_{1-x})_2O_3$ films grown on different planes of β-Ga_2O_3 substrates are accessed by high resolution XRD measurements. Figures 1(a)-(c) show the XRD ω-2θ scans from (020), (400) and $(\bar{6}03)$ reflections of β-$(Al_xGa_{1-x})_2O_3$ films grown along (010), (100) and $(\bar{2}01)$ orientations, respectively. The films were grown at growth temperature of 950 °C and chamber pressure of 60 Torr with different [TMAl]/[TMGa+TMAl] molar flow rate ratios as listed in Table 1. For all three orientations, the Al content in the films increases with the increase of [TMAl]/[TMGa+TMAl] molar flow rate ratio as indicated by the increase of the separation between the diffraction peaks corresponding to substrate and epi-films. The Al contents up to 29%, 99% and 16% are achieved in monoclinic $(Al_xGa_{1-x})_2O_3$ films grown on (010), (100) and $(\bar{2}01)$ oriented β-Ga_2O_3 substrates, respectively. The Al contents in β-$(Al_xGa_{1-x})_2O_3$ films are determined from the peak separation between the epilayer and the bulk β-Ga_2O_3 substrate [27, 40], assuming fully strained layers grown along various orientations, except for 62% and 99% Al content (100) $(Al_xGa_{1-x})_2O_3$ samples with thicknesses of 50 nm and 20 nm, respectively. For these two samples, the Al content is estimated based on the relaxed epitaxial layer grown on (100) β-Ga_2O_3 substrate [1], considering their lower critical thicknesses associated with such high Al contents [41]. The alloy contents extracted from high resolution XRD measurements correlate very closely with the Al contents estimated from STEM EDX elemental

mapping profiles and XPS measurements, as discussed later. For all β-$(Al_xGa_{1-x})_2O_3$ films grown along different orientations, the XRD peak intensity decreases as the Al content increases, indicating a degradation of the crystalline quality of the films with higher Al contents. However, the peak intensity of β-$(Al_xGa_{1-x})_2O_3$ films with larger Al contents may also have been reduced in part due to the lower x-ray scattering factor of Al relative to that of the Ga atom [42].

The XRD asymmetrical reciprocal space mapping (RSM) was used to analyze the strain state and growth coherence of β-$(Al_xGa_{1-x})_2O_3$ films grown on differently oriented β-Ga_2O_3 substrates. Figures 2 (a)-(c) show the asymmetrical RSMs for (420), (710) and ($\bar{4}$03) reflections of β-$(Al_xGa_{1-x})_2O_3$ films grown on (010), (100) and ($\bar{2}$01) oriented β-Ga_2O_3 substrates with 15%, 16% and 13% Al contents, respectively. The identical Q_x values for the peak positions from β-$(Al_xGa_{1-x})_2O_3$ films and β-Ga_2O_3 substrate indicate that the epitaxial layers with thicknesses of approximately 350 nm (on (010) β-Ga_2O_3 substrate), 120 nm (on (100) β-Ga_2O_3 substrate) and 205 nm (on $\bar{2}$01) β-Ga_2O_3 substrate) exhibit the same in-plane lattice constant as the substrate. This suggests that the β-$(Al_xGa_{1-x})_2O_3$ layers are fully strained and grow coherently on top of β-Ga_2O_3 substrate. While the films reveal coherent growth on differently oriented β-Ga_2O_3 substrates, a systematic growth study on the evaluation of the thickness limitations depending on the Al content and substrate orientations is of utmost importance for device applications. The recent theoretical DFT calculations predicted a strong influence of film orientation on the critical thicknesses of β-$(Al_xGa_{1-x})_2O_3$ films grown on differently oriented β-Ga_2O_3 substrates as a function of Al content [41]. The study revealed that the (100) oriented β-$(Al_xGa_{1-x})_2O_3$ films possess the largest critical thickness. However, from our previous experimental studies, the critical thickness of AlGaO grown on Ga_2O_3 is much thicker as compared to the theoretical predicted values, which can be related to the defects generated in the grown films [13]. The generation of the defects (such as Al

segregation) in high-Al AlGaO enables the growth of much thicker AlGaO films that are fully strained. The exact mechanisms still require further investigation.

The FESEM imaging was performed to investigate the surface morphology of the β-$(Al_xGa_{1-x})_2O_3$ films grown on β-Ga_2O_3 substrate with various Al contents. Figures 3 (a)-(i) show the surface FESEM images of β-$(Al_xGa_{1-x})_2O_3$ films grown on (010), (100) and $(\bar{2}01)$ β-Ga_2O_3 substrates with x = 15%, 29% and 54% (for (010) orientation), x = 16%, 28% and 99% (for (100) orientation), and x = 10%, 13% and 16% (for $(\bar{2}01)$ orientation). For the (010) oriented β-$(Al_xGa_{1-x})_2O_3$ film with 15% Al content, a smooth surface morphology is observed as shown in Figure 3(a). However, as the Al content increases to 29%, granular surface morphology is observed, which is likely due to the emergence of mixed phases (β plus γ phases) in the $(Al_xGa_{1-x})_2O_3$ film, as shown in XRD spectra in Figure 1 (a). Nevertheless, the surface of the $(Al_xGa_{1-x})_2O_3$ film becomes smoother as the Al content increases to 54%, which is attributed to a complete phase transformation from β to γ phase in the film [12]. The surface morphologies of (100) oriented β-$(Al_xGa_{1-x})_2O_3$ films with 16% and 28% Al content are shown in Figures 3(d) and 3(e), revealing smooth surfaces with distinctive three-dimensional (3D) structures. This can be attributed to the lack of energetically favorable nucleation sites for Ga adatoms, causing them to attach to other Ga adatoms and form islands, leading to the formation of 3D structures [15]. In a previous investigation involving homoepitaxial growth of (100) β-Ga_2O_3 films on substrates with miscut angles less than 2°, it was observed that the growth resulted in the formation of two-dimensional islands [43]. On on-axis substrates (or miscut angles smaller than 2°), the absence of energetically favorable kink sites on the surface step caused the formation of two-dimensional islands. As the miscut angle increased, step meandering occurred, eventually transitioning to step flow growth. In case of monoclinic $(Al_xGa_{1-x})_2O_3$ films with 99% Al content as shown in Figure 3(f), the surface uniformity significantly improves. While

there are no surface steps on on-axis substrates, during the growth of $(Al_xGa_{1-x})_2O_3$, the Al adatoms provides more nucleation sites for incoming adatoms, suppressing the 2D island growth mode and leading to a smoother, more uniform surface morphology [15]. On the other hand, the surface morphologies of $(\bar{2}01)$ oriented β-$(Al_xGa_{1-x})_2O_3$ films as shown in Figures 3 (g)-(i) exhibit granular surface features for different Al contents ranging between 10% and 16%.

Figures 4(a)-(i) show the corresponding surface AFM images (5 μm × 5 μm) of β-$(Al_xGa_{1-x})_2O_3$ films grown on (010), (100) and $(\bar{2}01)$ β-Ga_2O_3 substrates with different Al contents. In the case of (010) oriented β-$(Al_xGa_{1-x})_2O_3$ films, the surface RMS roughness values increase from 0.86 nm to 9.19 nm with an increase of Al content from 15% to 29%, as shown in Figure 4(a) and (b) due to the appearance of mixed phases. However, as the Al content further increases to 54%, the transformation from mixed phases (β plus γ phases) to single γ-phase $(Al_xGa_{1-x})_2O_3$ results in smoother surface morphology with smaller RMS roughness, as shown in Figure 4(c). Similarly, as the Al content increases from 16% to 28%, the surface of (100) β-$(Al_xGa_{1-x})_2O_3$ films becomes rougher due to the formation of three-dimensional (3D) structures on the growth surface as shown in Figures 4(d) and 4(e) (although film thickness reduces from 120 nm to 71 nm). The further increase of Al content to 99% significantly improves the surface uniformity with reduced RMS roughness (Figure 4(f)), which is consistent with the SEM image of Figure 3(f). In the case of $(\bar{2}01)$ oriented β-$(Al_xGa_{1-x})_2O_3$ films, the surface RMS roughness monotonically increases with the increase of Al contents as shown in Figures 4 (g)-(i).

High-resolution STEM imaging was employed to analyze the crystalline quality of the β-$(Al_xGa_{1-x})_2O_3$ thin films and β-$(Al_xGa_{1-x})_2O_3/Ga_2O_3$ SL structures grown on β-Ga_2O_3 substrates. The cross-sectional HAADF-STEM images of (010) β-$(Al_xGa_{1-x})_2O_3$ film with 15% Al content, as shown in Figures 5(a)-(b), reveal undisturbed monoclinic β-phase structures without any phase

transformation. The high-quality interface between the (010) β-Ga_2O_3 substrate (bright) and β-$(Al_xGa_{1-x})_2O_3$ epi-film (dark) is indicated by the sharp contrasts as observed in the STEM images. A uniform cross section of β-$(Al_xGa_{1-x})_2O_3$ layer without extended defects is observed in Figure 5(b), revealing high quality epitaxial growth of (010) β-$(Al_xGa_{1-x})_2O_3$ film with x = 15%. STEM-EDX mapping as shown in Figures 5 (c)-(d) was conducted on the corresponding β-$(Al_xGa_{1-x})_2O_3$ layer grown with 15% Al content to evaluate its compositional homogeneity and Al content. The Ga (green) and Al (blue) EDX color maps in Figures 5(c) indicate no compositional segregations in the epitaxial layer. The EDX elemental mapping of Ga and Al atoms in Figure 5 (d) also confirm uniform Al distribution throughout the β-$(Al_xGa_{1-x})_2O_3$ film. The average Al content obtained from STEM-EDX elemental maps in Figure 5(d) agrees well with the values extracted from XRD measurements (x = 15%).

Additionally, the high resolution HAADF-STEM imaging was performed for the (010) β-$(Al_xGa_{1-x})_2O_3$ film grown with 29% Al compositions as shown in Figure 6. The cross-sectional STEM images at (a) 200 nm and (b) 100 nm scales reveal epitaxial growth of ~280 nm β-$(Al_{0.29}Ga_{0.71})_2O_3$ film with atomic resolution images from (c) blue marked β-$(Al_{0.29}Ga_{0.71})_2O_3$ film region and (d, e) green and red marked β-$(Al_{0.29}Ga_{0.71})_2O_3$/substrate interface regions, indicating the formation of planer defects closer to the interface region, as clearly observed from (e). The formation of such extended planer defects perpendicular to the growth direction was also observed previously in MOCVD grown β-$(Al_{0.40}Ga_{0.60})_2O_3$ film, resembled a γ-phase inclusion at the local level [30]. Density functional theory (DFT) calculations have also indicated that these planar defects exhibit local stability, and their formation enthalpy, in comparison to the β-phase, is reduced during higher Al incorporation [30]. The inset of (b) shows the nano diffraction patterns acquired from the film region (blue marked), revealing two distinct structures: one from the growth along [001]

imaging direction of the β-phase, exhibiting its (010) growth continued from the β-Ga_2O_3 substrate and another one is from a 90° rotation of the (010) β-$(Al_{0.29}Ga_{0.71})_2O_3$ film, producing [010] imaging orientation of the β-phase and indicating the growth of (001) β-$(Al_{0.29}Ga_{0.71})_2O_3$. The atomic resolution STEM imaging in (c) also reveals the domain rotation of β-$(Al_{0.29}Ga_{0.71})_2O_3$ film. The STEM-EDX atomic fraction elemental profile of Ga, Al and O atoms along the orange arrow in (a) reveals uniform Al incorporation of ~30%, which closely match with the Al content (29%) determined from XRD measurement.

Apart from the advancement of high-quality growth of β-$(Al_xGa_{1-x})_2O_3$ thin films, the β-$(Al_xGa_{1-x})_2O_3/Ga_2O_3$ superlattice (SL) structures are also highly significant in various applications due to their ability to engineer the bandgap by alternating Ga_2O_3 and $(Al_xGa_{1-x})_2O_3$ layers, enabling precise control over electronic properties for device applications. Additionally, these structures allow for strain engineering by carefully designing layer thicknesses, which can have a significant impact on material properties such as band structure and carrier transport. Moreover, the periodic alternation of Ga_2O_3 and $(Al_xGa_{1-x})_2O_3$ layers in superlattices helps mitigate defects, confining or terminating them at the interfaces, and improving the overall material quality. In addition to the epitaxial growth of β-$(Al_xGa_{1-x})_2O_3$ thin films, (010) β-$(Al_xGa_{1-x})_2O_3/Ga_2O_3$ SL structures with x = 12% and 20% are also investigated. The eight-period β-$(Al_xGa_{1-x})_2O_3/Ga_2O_3$ SL structures were grown with a targeted thickness of 15 nm for the β-$(Al_xGa_{1-x})_2O_3$ barrier layer and 15 nm for the β-Ga_2O_3 well layer. Figure 7(a) shows the XRD ω-2θ scan of two SL structures with Al contents of 12% and 20%. The uniformly spaced satellite peak patterns confirm the periodicity of the SL structures. The presence of sharp and well-defined high-order satellite peaks, along with a strong 0th order peak, indicates the presence of high quality sharp β-$(Al_xGa_{1-x})_2O_3/Ga_2O_3$ interfaces and uniform alloy distribution in the β-$(Al_xGa_{1-x})_2O_3$ layers. The SL period of 30.88 nm obtained using

the angular separation between two adjacent satellite peaks for β-$(Al_xGa_{1-x})_2O_3/Ga_2O_3$ SL structures with x = 20% agrees well with the value (31 nm) determined from the STEM images. Figures 7(b)-(c) display cross sectional STEM imaging of 20% Al content SL structure in 50 nm and 5 nm scales, respectively. The sharp contrast in high-resolution STEM imaging between β-$(Al_xGa_{1-x})_2O_3$ barrier and β-Ga_2O_3 well layers reveal abrupt interfaces throughout the entire structure as shown in Figure 7(b). No degradation in the interface quality is observed in the entire structure. The atomic resolution STEM image in Figure 7(c) exhibits highly homogeneous Al distributions in β-$(Al_xGa_{1-x})_2O_3$ layers without phase transformation or domain rotations, demonstrating excellent quality of (010) oriented β-$(Al_xGa_{1-x})_2O_3/Ga_2O_3$ SLs up to 20% Al content.

The structural quality of β-$(Al_xGa_{1-x})_2O_3$ film grown on $(\bar{2}01)$ oriented β-Ga_2O_3 substrates is also evaluated by STEM imaging as shown in Figures 8(a) and 8(b) for Al content of 13%. The cross sectional HAADF STEM image as shown in Figure 8(a) exhibits 220 nm thick β-$(Al_xGa_{1-x})_2O_3$ film grown on top of $(\bar{2}01)$ oriented β-Ga_2O_3 substrate with a distinct interface between β-$(Al_xGa_{1-x})_2O_3$ film and β-Ga_2O_3 substrate. The atomic resolution STEM image at the interface as shown in Figure 8(b) also reveals the epitaxial growth of $(\bar{2}01)$ oriented phase pure β-$(Al_xGa_{1-x})_2O_3$ film with abrupt interface between the film and substrate, and without any rotational domain and phase segregation. However, the β-$(Al_xGa_{1-x})_2O_3$ film grown on top of β-Ga_2O_3 substrate exhibits significant contrast tilted along (100) plane, suggesting an uneven distribution of Al. This nonuniform Al distribution was also observed in $(\bar{2}01)$ and (001) β-$(Al_xGa_{1-x})_2O_3$ films grown using TEGa as the Ga precursor [16, 19]. Such nonuniformity in the Al distribution in $(\bar{2}01)$ β-$(Al_xGa_{1-x})_2O_3$ film can be attributed to the highly anisotropic properties of β-gallia structure, particularly to its strong orientation dependent surface free energy of different planes [38].

To evaluate the Al content and uniformity within $(\bar{2}01)$ β-$(Al_xGa_{1-x})_2O_3$ film, STEM-EDX mapping was performed as shown in Figures 9 (a)-(e). The darker regions in Figure 9(a) are attributed to an increase in Al concentration, as demonstrated by the Al and Ga elemental maps shown in Figures 9(b) and 9(c), respectively. A line scan along the orange arrow in Figure 9(a) was conducted to determine the element concentration, as shown in Figure 9(e). The quantitative EDX elemental mapping indicates an average Al content of ~ 20%, which is higher as compared to the content (x = 13%) determined from XRD measurement. This can be attributed to the nonuniformity of Al distribution in the epilayer as observed from the cross-sectional STEM image in Figure 9(a).

Using atomic resolution STEM images as shown in Figures 10 (a)-(d), we also investigated the structure, defects, and content of β-$(Al_xGa_{1-x})_2O_3$ film with 16% Al content grown on (100) oriented β-Ga_2O_3 substrate. The cross sectional HAADF-STEM image in Figure 10(a) indicates high quality epitaxial growth of β-$(Al_xGa_{1-x})_2O_3$ film. With a higher magnification, the HAADF image in Figure 10(b) shows a sharp interface between β-$(Al_xGa_{1-x})_2O_3$ epitaxial film and β-Ga_2O_3 layer. However, extended defects are observed at the atomic scale, as shown in Figures 10(c) and 10(d). Figure 10(d) shows a common defect in β-Ga_2O_3 films grown on (100) oriented β-Ga_2O_3 substrates without or having small miscuts, known as a twin. This defect is indicated by a red-dashed line that corresponds to the twin boundary lying in the (100) plane. The twin is characterized by a mirror operation at the boundary plane and a translation in the $[001]_m$ direction. The use of the on-axis (100) substrates for the β-$(Al_xGa_{1-x})_2O_3$ films growth is anticipated to result in such twin formation. This type of twinning in (100) β-Ga_2O_3 and β-$(Al_xGa_{1-x})_2O_3$ films grown on on-axis β-Ga_2O_3 substrates has been reported in prior studies [15, 44, 45]. The STEM-EDX analysis on the same β-$(Al_xGa_{1-x})_2O_3$ film with 16% Al content also confirms the presence of abrupt

interfaces, as shown in Figs. 11(a)-(e), without compositional segregation. In addition, EDX elemental mapping also revealed uniform distribution of Al and Ga atoms throughout the films. The average Al content determined from the EDX elemental maps as shown in Figure 11(e) matches well with those extracted from XRD measurement.

We also employed atomic resolution STEM to assess the structure and content of the monoclinic $(Al_xGa_{1-x})_2O_3$ film with 99% Al content grown on (100) β-Ga_2O_3 substrate. The results obtained from HAADF-STEM imaging are presented in Figures 12(a)-(d). The images shown in Figures 12(a) and 12(b) demonstrate the epitaxial growth of ~20 nm thick (100) $(Al_{0.99}Ga_{0.01})_2O_3$ film with a sharp interface. Although there is no evidence of Al segregation in the film, atomic scale STEM image as shown in Figure 12(b) indicates the presence of rotational domains. Electron nano-diffraction was employed to investigate the crystal structures of $(Al_xGa_{1-x})_2O_3$ film, confirming the monoclinic growth with Al content of 99%. The electron diffraction pattern in Figure 12(c) reveal monoclinic $(Al_xGa_{1-x})_2O_3$ growth with the localized region with zone orientation of [010], but with an out-of-plane rotation of 180°. The simulated diffraction patterns of [010] β-Ga_2O_3 and $[0\bar{1}0]$ β-Ga_2O_3 (180° out-of-plane rotation) closely resemble with the experimental diffraction pattern, confirming monoclinic $(Al_xGa_{1-x})_2O_3$ thin film with the high Al content of 99%. STEM EDX mapping was carried out to further confirm the Al content in corresponding $(Al_xGa_{1-x})_2O_3$ film as shown in Figures 13 (a)-(e). The sharp interface and alloy homogeneity is observed from the EDX color maps of Al (blue) and Ga (green) elements. The quantitative elemental mapping in Figure 13(e) confirms an average Al content of 99% in monoclinic $(Al_xGa_{1-x})_2O_3$ film grown on (100) β-Ga_2O_3 substrate, which agrees well with the Al content extracted from XRD measurement.

The elemental contents of the (100) β-$(Al_xGa_{1-x})_2O_3$ films were further confirmed by investigating the XPS core level spectra. To determine the Al contents, the areas of Ga $2p_{3/2}$ and Al 2p core level spectra were utilized, after subtracting the Shirley background, and using relative sensitivity factors of Ga $2p_{3/2}$ ($S_{Ga\ 2p3/2}$ = 21.4) and Al 2p ($S_{Al\ 2p}$ = 0.5371) as shown in Figure 14. The Al contents in (100) $(Al_xGa_{1-x})_2O_3$ films were determined to be 15%, and 98%, which were also confirmed by measuring the area of Ga $2p_{1/2}$ ($S_{Ga\ 2p1/2}$ = 11.09), and Al 2s ($S_{Al\ 2s}$ = 0.753) core level spectra. The Al contents determined using XPS closely match with the Al contents estimated by XRD and STEM EDX elemental mapping.

The bandgap of the β-phase $(Al_xGa_{1-x})_2O_3$ are also determined by utilizing XPS. Numerous studies using XPS measurements have shown that the inelastic energy loss spectra can provide valuable information about the bandgap of wide-band-gap semiconductor materials [31, 46-49]. This is because the excitation of a photoelectron from the valence band to the conduction band as it traverses from the bulk to the surface represents the minimum threshold for inelastic scattering. Therefore, the onset of the inelastic loss spectra at the higher binding energy side of the core level peak corresponds to the bandgap energy [46]. In this work, the bandgaps of (100) $(Al_xGa_{1-x})_2O_3$ films with Al contents of 16% and 99% are determined using the O 1s core level peak, as shown in Figures 15 (a)-(b). The inset figure provides a closer look at the background region of the O 1s peak. The energy of the onset of inelastic loss spectra was determined by intersecting the linear fitting of the inelastic background to the constant background. By estimating the onset of inelastic loss relative to the O 1s peak, the bandgap for (100) $(Al_{0.16}Ga_{0.84})_2O_3$ and $(Al_{0.99}Ga_{0.01})_2O_3$ films were determined to be 5.15 ± 0.15 eV and 7.26 ± 0.15 eV, respectively. The error bars correspond to the standard deviation of the estimated onset of the inelastic losses. The bandgap energies

increase as the Al content increases, which closely agree with the theoretically predicted bandgap values [1].

Additionally, β-$(Al_xGa_{1-x})_2O_3$/Ga_2O_3 SL structure grown on (100) β-Ga_2O_3 substrate is also investigated to evaluate the structural and interfacial quality in β-$(Al_xGa_{1-x})_2O_3$ layer with targeted Al content of 59%. The XRD ω-2θ scan as shown in Figure 16(a) displays noticeable satellite peaks alongside the 0^{th} order peak, indicating that the structural periodicities are well-preserved despite the presence of high-Al content. Cross-sectional HAADF STEM images in Figures 16(b) and 16(c) show eight periods consisting of β-$(Al_xGa_{1-x})_2O_3$ and β-Ga_2O_3 sublayers. While the SL maintains pure β-phase throughout the structure, extended defects and twin-boundaries are observed from atomic scale image in Figure 16 (c), which can be attributed to its growth on on-axis (100) β-Ga_2O_3 substrate without miscut angles. STEM-EDX maps of the corresponding SL structure as shown in Figures 17(a)-(e) reveal compositional variation in different β-$(Al_xGa_{1-x})_2O_3$ layers. The quantitative elemental mapping in Figure 17(e) exhibits periodic structures with alternating compositional profiles with ~ 60% Al incorporation in the β-$(Al_xGa_{1-x})_2O_3$ layers.

According to the theoretical DFT calculations, the thermodynamically stable monoclinic β phase is expected to persist in $(Al_xGa_{1-x})_2O_3$ alloy up to at least 50% Al contents [50]. However, previous experimental studies on thin-film growth of $(Al_xGa_{1-x})_2O_3$ on (010) β-Ga_2O_3 substrates have shown phase segregation at Al concentrations well below 50% [12]. Nevertheless, the Al incorporation in β-phase $(Al_xGa_{1-x})_2O_3$ films were found to be highly dependent on the orientation of the β-Ga_2O_3 substrates [51]. Different orientations of β-Ga_2O_3 substrates resulted in different Al contents in β-$(Al_xGa_{1-x})_2O_3$. For example, the (100) β-$(Al_xGa_{1-x})_2O_3$ films were demonstrated with maximum Al content of 52% [15], whereas (001) oriented β-$(Al_xGa_{1-x})_2O_3$ films showed lowest Al content of 25% [19]. The orientation-dependent limitation on the maximum Al contents in β-$(Al_xGa_{1-}$

$_x)_2O_3$ can be attributed to the varying surface free energies of different planes [51]. The lower surface free energy leads to higher Al incorporation in β-$(Al_xGa_{1-x})_2O_3$, indicating that the β-Ga_2O_3 substrate with (100) plane with lowest surface free energy is the most favorable to incorporate higher Al contents. The experimental results in this study reveal almost 100% Al incorporation in monoclinic $(Al_xGa_{1-x})_2O_3$ thin films grown on (100) β-Ga_2O_3 substrate. Nonetheless, the maximum Al incorporation in β-$(Al_xGa_{1-x})_2O_3$ is still limited along other orientations, such as (010) and $(\bar{2}01)$, which suggests that the different surface free energies of various planes play a crucial role in incorporating different Al contents into the alloy. Although theoretical calculations suggest that the monoclinic β-phase $(Al_xGa_{1-x})_2O_3$ could be stabilized with up to 62.5% Al contents [50], it is more likely that the kinetic factors associated with the growth conditions play a significant role in achieving such high levels of Al incorporation in monoclinic β-$(Al_xGa_{1-x})_2O_3$ films. However, further investigations are required to determine the mechanisms that promote the formation of monoclinic $(Al_xGa_{1-x})_2O_3$ films with almost 100% Al contents during the MOCVD growth.

IV. Conclusion

In summary, this study systematically investigated the MOCVD epitaxial growth of β-$(Al_xGa_{1-x})_2O_3$ thin films and β-$(Al_xGa_{1-x})_2O_3$/β-Ga_2O_3 superlattice structures on differently oriented β-Ga_2O_3 substrates using TMGa as the Ga precursors. Extensive material characterizations utilizing XRD, XPS, STEM and EDX elemental mapping were performed on films grown on different oriented substrates with various Al contents. Single-phase monoclinic $(Al_xGa_{1-x})_2O_3$ films on (100), (010), and $(\bar{2}01)$ oriented β-Ga_2O_3 substrates have been demonstrated with Al contents reaching up to 99%, 29%, and 16%, respectively. However, when the Al incorporation surpasses 29%, (010) oriented β-$(Al_xGa_{1-x})_2O_3$ films exhibit β-to-γ phase segregation. The highly anisotropic nature of β-$(Al_xGa_{1-x})_2O_3$ films grown on $(\bar{2}01)$ β-Ga_2O_3

substrates results in local segregation of Al along the (100) plane. Incoherent twin boundary defects are observed in (100) β-$(Al_xGa_{1-x})_2O_3$ films grown on on-axis (100) β-Ga_2O_3 substrates. In this work, record high Al incorporation of up to 99% is confirmed in (100) monoclinic $(Al_xGa_{1-x})_2O_3$ film through various measurements, including XRD, STEM, electron nano-diffraction, and XPS. The successful MOCVD growth of β-$(Al_xGa_{1-x})_2O_3$ alloys with fast growth rates and Al contents along different orientations holds promises for the advancement of high power and high-frequency electronic and optoelectronic devices based on $(Al_xGa_{1-x})_2O_3$ films or β-$(Al_xGa_{1-x})_2O_3$/β-Ga_2O_3 heterostructures.

Acknowledgements

The authors acknowledge the Air Force Office of Scientific Research FA9550-18-1-0479 (AFOSR, Dr. Ali Sayir) for financial support. The authors also acknowledge the National Science Foundation (Grant No. 2231026, No. 2019753) and Semiconductor Research Corporation (SRC) under the Task ID GRC 3007.001 for partial support. The electron microscopy was performed at the Center for Electron Microscopy and Analysis (CEMAS) at The Ohio State University.

Data Availability

The data that support the findings of this study are available from the corresponding author upon reasonable request.

References

1. H. Peelaers, J. B. Varley, J. S. Speck and C. G. Van de Walle, Applied Physics Letters **112** (24), 242101 (2018).
2. M. Higashiwaki, K. Sasaki, A. Kuramata, T. Masui and S. Yamakoshi, Applied Physics Letters **100** (1), 013504 (2012).
3. Z. Feng, A. Anhar Uddin Bhuiyan, M. R. Karim and H. Zhao, Applied Physics Letters **114** (25), 250601 (2019).

4. Z. Feng, A. F. M. A. U. Bhuiyan, Z. Xia, W. Moore, Z. Chen, J. F. McGlone, D. R. Daughton, A. R. Arehart, S. A. Ringel, S. Rajan and H. Zhao, physica status solidi (RRL) – Rapid Research Letters **14** (8), 2000145 (2020).
5. L. Meng, Z. Feng, A. F. M. A. U. Bhuiyan and H. Zhao, Crystal Growth & Design **22** (6), 3896 (2022).
6. A. Kuramata, K. Koshi, S. Watanabe, Y. Yamaoka, T. Masui and S. Yamakoshi, Japanese Journal of Applied Physics **55** (12), 1202A2 (2016).
7. Z. Galazka, Journal of Applied Physics **131** (3) (2022).
8. K. Hoshikawa, T. Kobayashi and E. Ohba, Journal of Crystal Growth **546**, 125778 (2020).
9. Z. Galazka, A. Fiedler, A. Popp, S. Ganschow, A. Kwasniewski, P. Seyidov, M. Pietsch, A. Dittmar, S. B. Anooz and K. Irmscher, Journal of Applied Physics **133** (3) (2023).
10. J. B. Varley, Journal of Materials Research **36** (23), 4790 (2021).
11. A. F. M. Anhar Uddin Bhuiyan, Z. Feng, J. M. Johnson, Z. Chen, H.-L. Huang, J. Hwang and H. Zhao, Applied Physics Letters **115** (12), 120602 (2019).
12. A. F. M. A. U. Bhuiyan, Z. Feng, J. M. Johnson, H.-L. Huang, J. Sarker, M. Zhu, M. R. Karim, B. Mazumder, J. Hwang and H. Zhao, APL Materials **8** (3), 031104 (2020).
13. A. F. M. A. U. Bhuiyan, Z. Feng, L. Meng and H. Zhao, Journal of Materials Research **36** (23), 4804 (2021).
14. A. F. M. A. U. Bhuiyan, Z. Feng, L. Meng, A. Fiedler, H.-L. Huang, A. T. Neal, E. Steinbrunner, S. Mou, J. Hwang, S. Rajan and H. Zhao, Journal of Applied Physics **131** (14), 145301 (2022).
15. A. F. M. Anhar Uddin Bhuiyan, Z. Feng, J. M. Johnson, H.-L. Huang, J. Hwang and H. Zhao, Crystal Growth & Design **20** (10), 6722 (2020).
16. A. F. M. A. U. Bhuiyan, Z. Feng, J. M. Johnson, H.-L. Huang, J. Hwang and H. Zhao, Applied Physics Letters **117** (14), 142107 (2020).
17. J. B. Varley, A. Perron, V. Lordi, D. Wickramaratne and J. L. Lyons, Applied Physics Letters **116** (17), 172104 (2020).
18. A. F. M. A. U. Bhuiyan, L. Meng, H.-L. Huang, J. Sarker, M. Zhu, B. Mazumder, J. Hwang and H. Zhao, in *IWGO (Japan)* (2022).
19. A. F. M. A. U. Bhuiyan, L. Meng, H.-L. Huang, J. Sarker, C. Chae, B. Mazumder, J. Hwang and H. Zhao, APL Mater 11, 041112 (2023).
20. S. Krishnamoorthy, Z. Xia, C. Joishi, Y. Zhang, J. McGlone, J. Johnson, M. Brenner, A. R. Arehart, J. Hwang, S. Lodha and S. Rajan, Applied Physics Letters **111** (2), 023502 (2017).
21. Y. Zhang, A. Neal, Z. Xia, C. Joishi, J. M. Johnson, Y. Zheng, S. Bajaj, M. Brenner, D. Dorsey, K. Chabak, G. Jessen, J. Hwang, S. Mou, J. P. Heremans and S. Rajan, Applied Physics Letters **112** (17), 173502 (2018).
22. P. Ranga, A. Bhattacharyya, A. Chmielewski, S. Roy, R. Sun, M. A. Scarpulla, N. Alem and S. Krishnamoorthy, Applied Physics Express **14** (2), 025501 (2021).
23. P. P. Sundaram, F. Alema, A. Osinsky and S. J. Koester, Journal of Vacuum Science & Technology A **40** (4), 043211 (2022).

24. H.-H. Wan, J.-S. Li, C.-C. Chiang, X. Xia, F. Ren, H. N. Masten, J. S. Lundh, J. A. Spencer, F. Alema, A. Osinsky, A. G. Jacobs, K. Hobart, M. J. Tadjer and S. J. Pearton, Journal of Vacuum Science & Technology A **41** (3), 032701 (2023).
25. K. Ghosh and U. Singisetti, Journal of Materials Research **32** (22), 4142 (2017).
26. S. W. Kaun, F. Wu and J. S. Speck, Journal of Vacuum Science & Technology A: Vacuum, Surfaces, and Films **33** (4), 041508 (2015).
27. A. Mauze, T. Itoh, Y. Zhang, E. Deagueros, F. Wu and J. S. Speck, Journal of Applied Physics **132** (11), 115302 (2022).
28. J. Sarker, S. Broderick, A. F. M. A. U. Bhuiyan, Z. Feng, H. Zhao and B. Mazumder, Applied Physics Letters **116** (15), 152101 (2020).
29. A. F. M. A. U. Bhuiyan, Z. Feng, J. M. Johnson, H.-L. Huang, J. Sarker, M. Zhu, M. R. Karim, B. Mazumder, J. Hwang and H. Zhao, APL Materials **8** (8), 089102 (2020).
30. J. M. Johnson, H.-L. Huang, M. Wang, S. Mu, J. B. Varley, A. F. M. A. Uddin Bhuiyan, Z. Feng, N. K. Kalarickal, S. Rajan, H. Zhao, C. G. Van de Walle and J. Hwang, APL Materials **9** (5), 051103 (2021).
31. A. F. M. A. U. Bhuiyan, Z. Feng, H.-L. Huang, L. Meng, J. Hwang and H. Zhao, APL Materials **9** (10), 101109 (2021).
32. J. Sarker, A. A. U. Bhuiyan, Z. Feng, H. Zhao and B. Mazumder, Journal of Physics D: Applied Physics **54** (18), 184001 (2021).
33. P. Ranga, A. Rishinaramangalam, J. Varley, A. Bhattacharyya, D. Feezell and S. Krishnamoorthy, Appl. Phys. Express **12** 111004 (2019).
34. A. F. M. A. U. Bhuiyan, L. Meng, H.-L. Huang, J. Hwang and H. Zhao, Journal of Applied Physics 132, 165301 (2022).
35. A. F. M. A. U. Bhuiyan, Z. Feng, H.-L. Huang, L. Meng, J. Hwang and H. Zhao, Journal of Vacuum Science & Technology A **39** (6), 063207 (2021).
36. V. Hill, R. Roy and E. Osborn, Journal of the American Ceramic Society **35** (6), 135 (1952).
37. A. F. M. A. U. Bhuiyan, Z. Feng, J. M. Johnson, H.-L. Huang, J. Hwang and H. Zhao, Applied Physics Letters **117** (25), 252105 (2020).
38. S. Mu, H. Peelaers, Y. Zhang, M. Wang and C. G. Van de Walle, Applied Physics Letters **117** (25), 252104 (2020).
39. M. Baldini, M. Albrecht, A. Fiedler, K. Irmscher, D. Klimm, R. Schewski and G. Wagner, Journal of Materials Science 51 (7), 3650 (2016).
40. Y. Oshima, E. Ahmadi, S. C. Badescu, F. Wu and J. S. Speck, Applied Physics Express **9** (6), 061102 (2016).
41. S. Mu, M. Wang, H. Peelaers and C. G. Van de Walle, APL Materials **8** (9), 091105 (2020).
42. K. Kaneko, K. Suzuki, Y. Ito and S. Fujita, Journal of Crystal Growth **436**, 150 (2016).
43. R. Schewski, M. Baldini, K. Irmscher, A. Fiedler, T. Markurt, B. Neuschulz, T. Remmele, T. Schulz, G. Wagner, Z. Galazka and M. Albrecht, Journal of Applied Physics **120** (22), 225308 (2016).

44. R. Schewski, K. Lion, A. Fiedler, C. Wouters, A. Popp, S. V. Levchenko, T. Schulz, M. Schmidbauer, S. Bin Anooz, R. Grüneberg, Z. Galazka, G. Wagner, K. Irmscher, M. Scheffler, C. Draxl and M. Albrecht, APL Materials **7** (2), 022515 (2019).
45. A. Fiedler, R. Schewski, M. Baldini, Z. Galazka, G. Wagner, M. Albrecht and K. Irmscher, Journal of Applied Physics **122** (16), 165701 (2017).
46. M. T. Nichols, W. Li, D. Pei, G. A. Antonelli, Q. Lin, S. Banna, Y. Nishi and J. L. Shohet, Journal of Applied Physics **115** (9), 094105 (2014).
47. T. Kamimura, K. Sasaki, M. Hoi Wong, D. Krishnamurthy, A. Kuramata, T. Masui, S. Yamakoshi and M. Higashiwaki, Applied Physics Letters **104** (19), 192104 (2014).
48. F. Zhang, K. Saito, T. Tanaka, M. Nishio, M. Arita and Q. Guo, Applied Physics Letters **105** (16), 162107 (2014).
49. C. Fares, F. Ren, E. Lambers, D. C. Hays, B. P. Gila and S. J. Pearton, Journal of Vacuum Science & Technology B **36** (6), 061207 (2018).
50. S. Mu and C. G. Van de Walle, Physical Review Materials **6** (10), 104601 (2022).
51. A. F. M. A. U. Bhuiyan, Z. Feng, L. Meng and H. Zhao, Journal of Applied Physics 133, 211103 (2023).

Figure Captions

Figure 1. XRD ω-2θ scan profiles of the (a) (020), (b) (400), and (c) ($\bar{6}03$) reflections of β-$(Al_xGa_{1-x})_2O_3$ films grown on (010), (100) and ($\bar{2}01$) β-Ga_2O_3 substrates with Al incorporations up to 29%, 99% and 16%, respectively.

Figure 2. Asymmetrical reciprocal space maps (RSMs) around (a) (420), (b) (710), and (c) ($\bar{4}03$) reflections of (010), (100) and ($\bar{2}01$) β-$(Al_xGa_{1-x})_2O_3$ films with x = 15%, 16%, and 13% respectively.

Figure 3. Surface view FESEM images of β-$(Al_xGa_{1-x})_2O_3$ films grown on (a-c) (010), (d-f) (100) and (g-i) ($\bar{2}01$) oriented β-Ga_2O_3 substrates with different Al contents.

Figure 4. Surface AFM images of β-$(Al_xGa_{1-x})_2O_3$ films grown on (a-c) (010), (d-f) (100) and (g-i) ($\bar{2}01$) oriented β-Ga_2O_3 substrates with different Al contents.

Figure 5. High resolution cross-sectional HAADF-STEM images of (010) β-$(Al_xGa_{1-x})_2O_3$ film with 15% Al contents at (a) 200 nm, (b) 5 nm, and (b) 1 nm scales, showing homogenous and uniform β-$(Al_xGa_{1-x})_2O_3$ layer with sharp interface. The HAADF-STEM images were taken from the < 010 > zone axes. (d) Cross-sectional HAADF image of β-$(Al_{0.15}Ga_{0.85})_2O_3$ film with corresponding STEM-EDX mapping of (e) Ga, Al and O atoms. (e) Atomic fraction elemental profile along the orange arrow in (d).

Figure 6. High resolution cross-sectional HAADF-STEM images of (010) β-$(Al_xGa_{1-x})_2O_3$ film with 29% Al compositions at (a) 200 nm and (b) 100 nm scales with atomic resolution images of (c) blue marked β-$(Al_{0.29}Ga_{0.71})_2O_3$ film region and (d, e) green and red marked β-$(Al_{0.29}Ga_{0.71})_2O_3$/substrate interface region, indicating formation of planer defects closer to the interface region (e). The inset of (b) shows the nano diffraction patterns acquired from the film

region (blue marked), revealing two distinct structures: one from the growth along [001] imaging direction of the β-phase, exhibiting its (010) growth continued from the β-Ga_2O_3 substrate and another one is from a 90° rotation of the (010) β-$(Al_{0.29}Ga_{0.71})_2O_3$ film, producing [010] imaging orientation of the β-phase, indicating the growth of (001) β-$(Al_{0.29}Ga_{0.71})_2O_3$. The HAADF-STEM images were taken from the < 010 > zone axes. STEM-EDX atomic fraction elemental profile of Ga, Al and O atoms along the orange arrow in (a) reveals uniform Al incorporation of 30%.

Figure 7. (a) XRD ω-2θ scan of 8 period β-$(Al_xGa_{1-x})_2O_3$/β-Ga_2O_3 SLs grown on (010) β-Ga_2O_3 substrates with Al content of 20% and 12%. High resolution HAADF-STEM images of the corresponding SLs at (b) 50 nm, and (c) 5 nm scales, showing homogenous and uniform β-$(Al_xGa_{1-x})_2O_3$ layer with sharp interfaces.

Figure 8. (a) High resolution cross-sectional HAADF-STEM images of $(\bar{2}01)$ β-$(Al_xGa_{1-x})_2O_3$ film with 13% Al contents, showing Al distribution pattern along (100) plane. (b) Atomic resolution cross sectional image shows sharp interface between β-$(Al_xGa_{1-x})_2O_3$ and β-Ga_2O_3 layer.

Figure 9. STEM-EDX mapping of $(\bar{2}01)$ β-$(Al_{0.13}Ga_{0.87})_2O_3$ film (a) Cross-sectional HAADF image with corresponding EDX mapping of (b) Al, (c) Ga and (d) O atoms. (e) Atomic fraction elemental profile along the orange arrow in (a).

Figure 10. (a) High resolution HAADF-STEM images taken from the $[010]_m$ zone axis of β-$(Al_{0.16}Ga_{0.84})_2O_3$ film grown on top of an on-axis (100) β-Ga_2O_3 substrate. (b) and (c) represent high magnification images at β-$(Al_{0.16}Ga_{0.84})_2O_3$ film and interface regions, respectively. (d) Atomic resolution image of the β-$(Al_{0.16}Ga_{0.84})_2O_3$ film, showing twin boundary defects.

Figure 11. STEM-EDX mapping of (100) β-$(Al_{0.16}Ga_{0.84})_2O_3$ film (a) Cross-sectional HAADF image with corresponding EDX mapping of (b) Al, (c) Ga and (d) O atoms. (e) Atomic fraction

elemental profile along the orange arrow in (a), showing an average Al content of ~16% in the epilayer.

Figure 12. (a) High resolution HAADF-STEM images taken from the $[010]_m$ zone axis of monoclinic $(Al_{0.99}Ga_{0.01})_2O_3$ film grown on top of an on-axis (100) β-Ga_2O_3 substrate. (b) High magnification STEM images of $(Al_{0.99}Ga_{0.01})_2O_3$ film. Electron nano-diffraction pattern obtained from the (c) $(Al_{0.99}Ga_{0.01})_2O_3$ film and (d) simulation.

Figure 13. STEM-EDX mapping of (100) monoclinic $(Al_{0.99}Ga_{0.01})_2O_3$ film (a) Cross-sectional HAADF image with corresponding EDX mapping of (b) Al, (c) Ga and (d) O atoms. (e) Atomic fraction elemental profile along the orange arrow in (a), confirming an average Al content of ~99% in the epilayer.

Figure 14. Fitted Ga $2p_{3/2}$ and Al 2p core level spectra from (100) oriented (a) $(Al_{0.99}Ga_{0.01})_2O_3$ and (b) $(Al_{0.16}Ga_{0.84})_2O_3$ films after applying the Shirley background subtraction. The Al contents determined by comparing the areas of Ga $2p_{3/2}$ and Al 2p core level peaks match well with the contents extracted from STEM-EDX mapping and XRD.

Figure 15. (a) O 1s core level spectra of (100) oriented $(Al_xGa_{1-x})_2O_3$ films with Al content (a) x = 16% and (b) x = 99%. The inset shows the zoomed view of the inelastic background region marked by the black dashed rectangle in O 1s spectra. The bandgaps of 5.15 ± 0.15 eV and 7.26 ± 0.15 eV are calculated for x = 16% and x = 99%, respectively by using the binding energy difference between the O 1s core-level peak positions and the onsets of the inelastic backgrounds.

Figure 16. (a) XRD ω-2θ scan of 8 period β-$(Al_xGa_{1-x})_2O_3$/β-Ga_2O_3 SLs grown on (100) β-Ga_2O_3 substrates with Al content of 59%. High resolution HAADF-STEM images of the corresponding SLs at (b) 10 nm, and (c) 5 nm scales, showing inhomogeneous Al distribution in β-$(Al_xGa_{1-x})_2O_3$ layers.

Figure 17. STEM-EDX mapping of (100) β-$(Al_xGa_{1-x})_2O_3$/β-Ga_2O_3 superlattice structure grown with targeted Al contents of 59% (a) Cross-sectional HAADF image with corresponding EDX mapping of (b) Al, (c) Ga and (d) O atoms. (e) Atomic fraction elemental profile along the orange arrow in (a), showing 8 periods of the SL structure.

Table 1

Summary of β-$(Al_xGa_{1-x})_2O_3$ samples (as shown in Figure. 1) grown with different [TMAl]/[TMAl + TMGa] molar flow rate ratios with corresponding Al contents, film thicknesses and growth rates.

Sample ID	β-$(Al_xGa_{1-x})_2O_3$ film orientation	[TMAl]/[TMAl+TMGa] (%)	Film Thickness (nm)	Growth rates (μm/hr)	Al content (%)
1	(010)	3.01	353	2.12	5.4
2	(010)	5.66	360	2.16	9.2
3	(010)	12.93	358	2.15	15
4	(010)	15.78	422	2.53	19.7
5	(010)	18.49	280	1.68	29 (β+γ)
6	(010)	25.52	255	1.53	54 (γ)
7	(100)	8.03	120	1.80	16
8	(100)	12.93	131	1.57	21
9	(100)	18.49	71	2.13	28
10	(100)	22.65	142	2.13	33
11	(100)	24.03	50	1.50	62
12	(100)	26.9	20	1.20	99
13	$(\bar{2}01)$	6.88	155	1.86	10
14	$(\bar{2}01)$	18.49	131	1.57	16

Figure 1

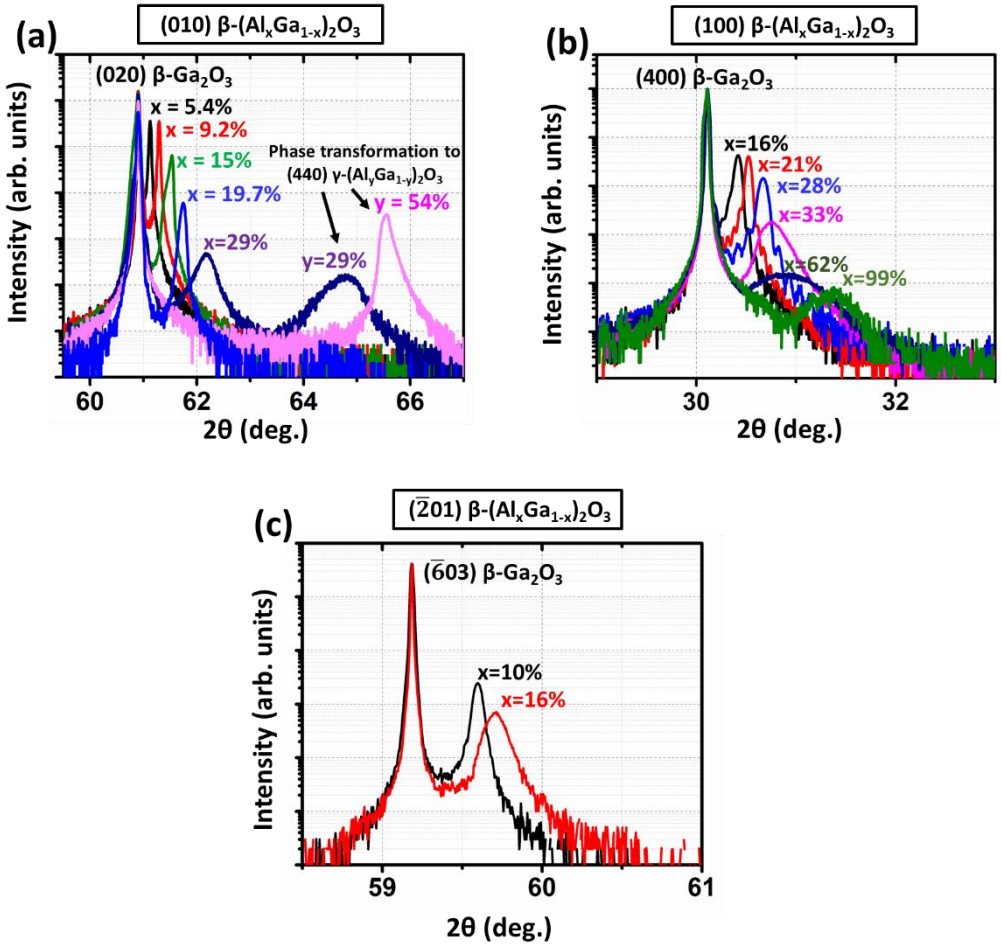
(a)
(010) β-(AlxGa1-x)2O3
(020) β-Ga2O3
x = 5.4%
x = 9.2%
x = 15%
x = 19.7%
x=29%
Phase transformation to
(440) γ-(AlyGa1-y)2O3
y=29%
y = 54%
Intensity (arb. units)
60
62
64
66
2θ (deg.)
(b)
(100) β-(AlxGa1-x)2O3
(400) β-Ga2O3
x=16%
x=21%
x=28%
x=33%
x=62%
x=99%
Intensity (arb. units)
30
32
2θ (deg.)
(c)
(2̄01) β-(AlxGa1-x)2O3
(6̄03) β-Ga2O3
x=10%
x=16%
Intensity (arb. units)
59
60
61
2θ (deg.)

Figure 2

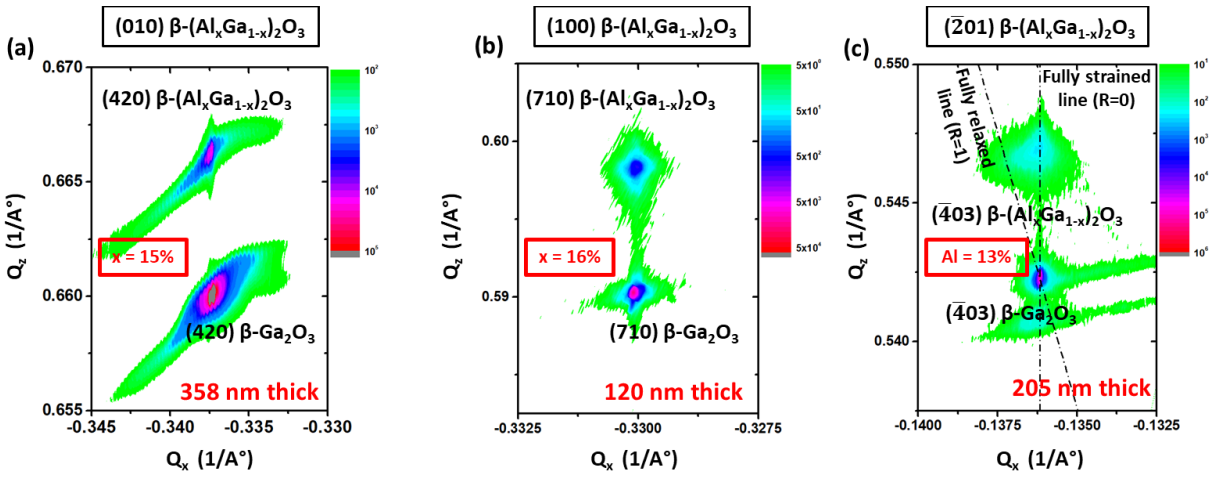
(a)
(010) β-(AlxGa1-x)2O3
(420) β-(AlxGa1-x)2O3
x = 15%
(420) β-Ga2O3
358 nm thick
0.670
0.665
0.660
0.655
-0.345
-0.340
-0.335
-0.330
Qz (1/A°)
Qx (1/A°)
(b)
(100) β-(AlxGa1-x)2O3
(710) β-(AlxGa1-x)2O3
x = 16%
(710) β-Ga2O3
120 nm thick
0.60
0.59
-0.3325
-0.3300
-0.3275
Qz (1/A°)
Qx (1/A°)
(c)
(2̄01) β-(AlxGa1-x)2O3
Fully relaxed line (R=1)
Fully strained line (R=0)
(4̄03) β-(AlxGa1-x)2O3
Al = 13%
(4̄03) β-Ga2O3
205 nm thick
0.550
0.545
0.540
-0.1400
-0.1375
-0.1350
-0.1325
Qz (1/A°)
Qx (1/A°)

Figure 3

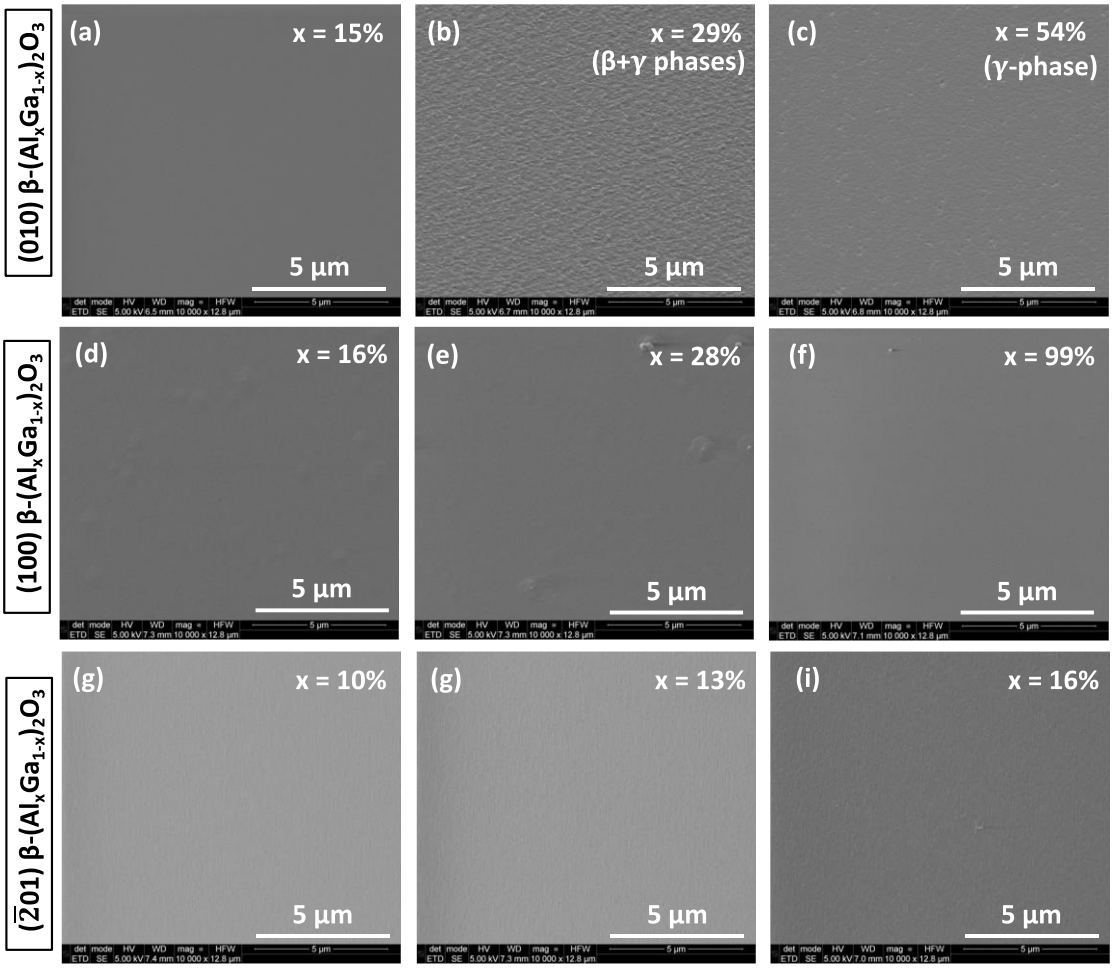
(010) β-(Al$_x$Ga$_{1-x}$)$_2$O$_3$
(a)
x = 15%
5 µm
(b)
x = 29%
(β+γ phases)
5 µm
(c)
x = 54%
(γ-phase)
5 µm
(100) β-(Al$_x$Ga$_{1-x}$)$_2$O$_3$
(d)
x = 16%
5 µm
(e)
x = 28%
5 µm
(f)
x = 99%
5 µm
(2̄01) β-(Al$_x$Ga$_{1-x}$)$_2$O$_3$
(g)
x = 10%
5 µm
(g)
x = 13%
5 µm
(i)
x = 16%
5 µm

Figure 4

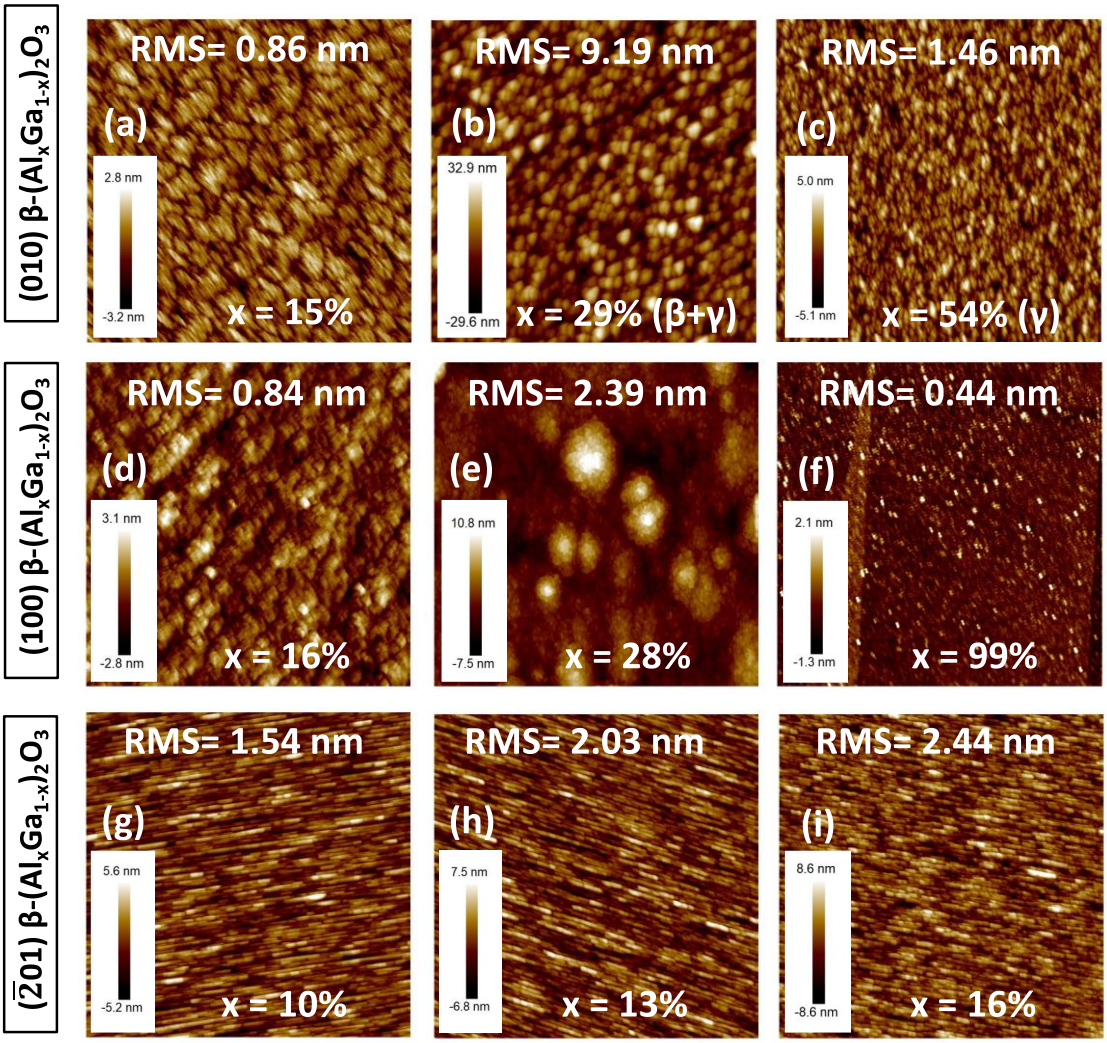
(010) β-(AlxGa1-x)2O3
RMS= 0.86 nm
(a)
2.8 nm
-3.2 nm
x = 15%
RMS= 9.19 nm
(b)
32.9 nm
-29.6 nm
x = 29% (β+γ)
RMS= 1.46 nm
(c)
5.0 nm
-5.1 nm
x = 54% (γ)
(100) β-(AlxGa1-x)2O3
RMS= 0.84 nm
(d)
3.1 nm
-2.8 nm
x = 16%
RMS= 2.39 nm
(e)
10.8 nm
-7.5 nm
x = 28%
RMS= 0.44 nm
(f)
2.1 nm
-1.3 nm
x = 99%
(2̄01) β-(AlxGa1-x)2O3
RMS= 1.54 nm
(g)
5.6 nm
-5.2 nm
x = 10%
RMS= 2.03 nm
(h)
7.5 nm
-6.8 nm
x = 13%
RMS= 2.44 nm
(i)
8.6 nm
-8.6 nm
x = 16%

Figure 5

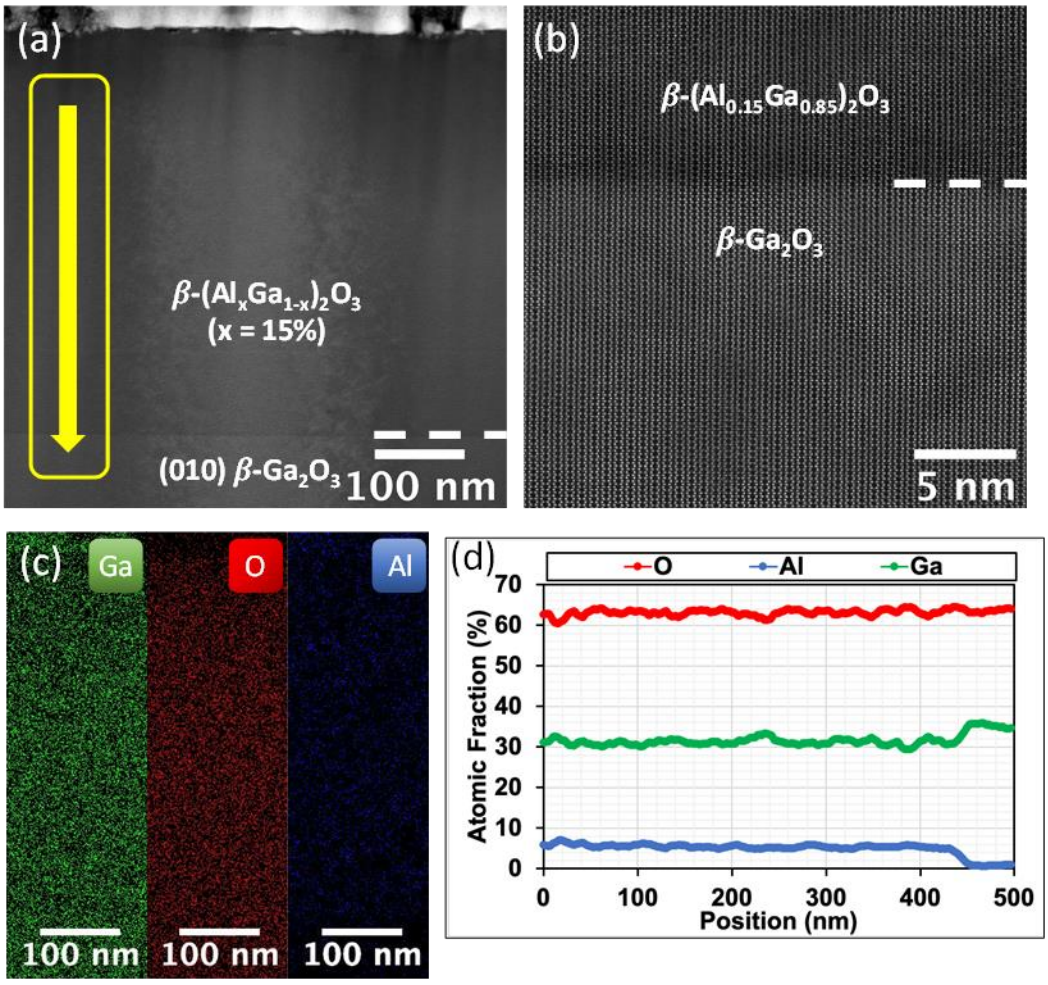
(a)
β-(AlxGa1-x)2O3
(x = 15%)
(010) β-Ga2O3
100 nm
(b)
β-(Al0.15Ga0.85)2O3
β-Ga2O3
5 nm
(c)
Ga
O
Al
100 nm
100 nm
100 nm
(d)
O
Al
Ga
Atomic Fraction (%)
0
10
20
30
40
50
60
70
0
100
200
300
400
500
Position (nm)

Figure 6

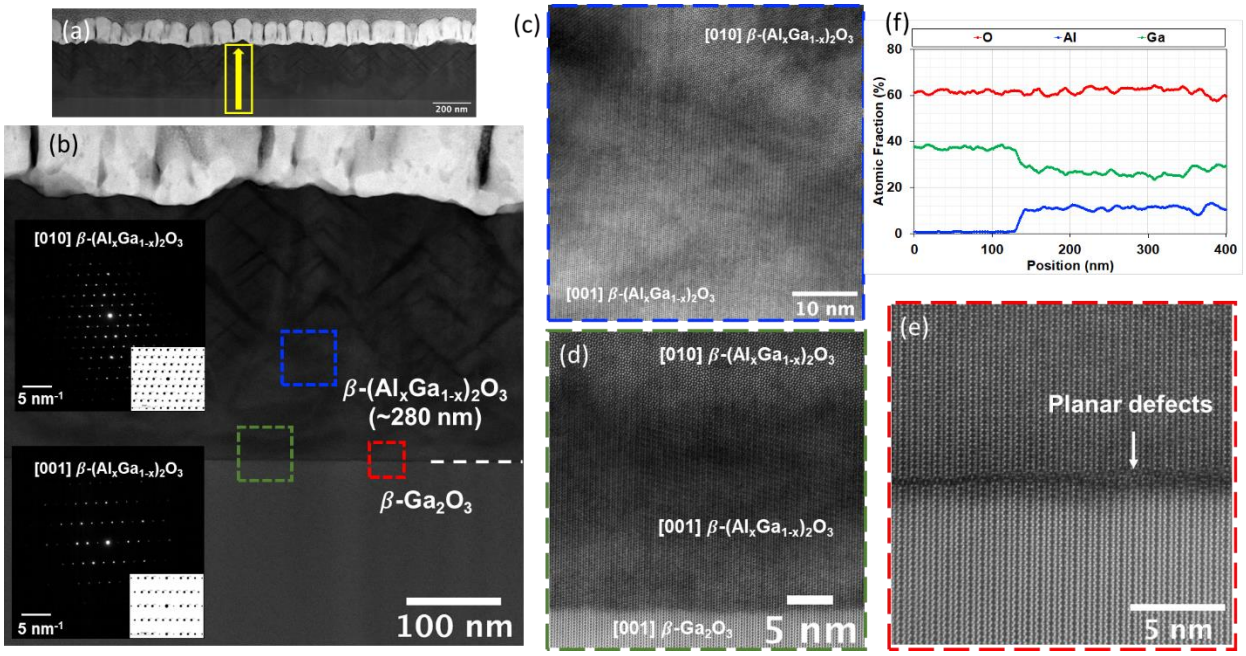
(a)
200 nm
(b)
[010] β-(AlxGa1-x)2O3
5 nm-1
[001] β-(AlxGa1-x)2O3
5 nm-1
β-(AlxGa1-x)2O3
(~280 nm)
β-Ga2O3
100 nm
(c)
[010] β-(AlxGa1-x)2O3
[001] β-(AlxGa1-x)2O3
10 nm
(d)
[010] β-(AlxGa1-x)2O3
[001] β-(AlxGa1-x)2O3
[001] β-Ga2O3
5 nm
(e)
Planar defects
5 nm
(f)
O
Al
Ga
Atomic Fraction (%)
Position (nm)

Figure 7

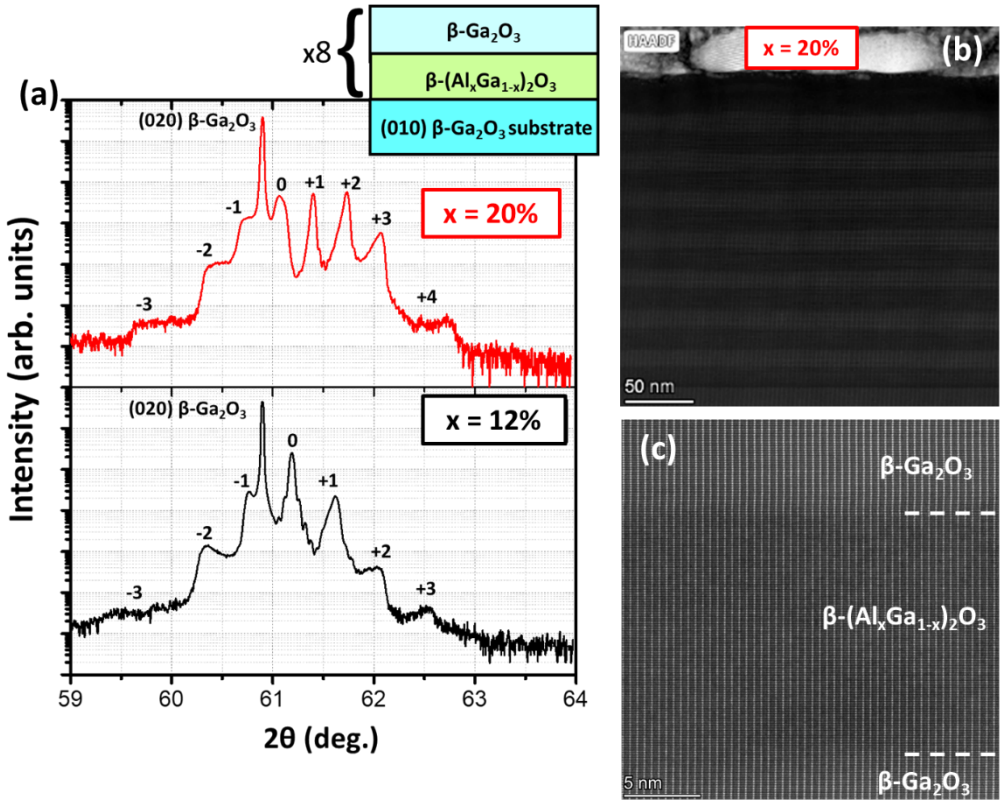
(a)
x8
β-Ga2O3
β-(AlxGa1-x)2O3
(010) β-Ga2O3 substrate
(020) β-Ga2O3
x = 20%
-3
-2
-1
0
+1
+2
+3
+4
(020) β-Ga2O3
x = 12%
-3
-2
-1
0
+1
+2
+3
Intensity (arb. units)
59
60
61
62
63
64
2θ (deg.)
HAADF
x = 20%
(b)
50 nm
(c)
β-Ga2O3
β-(AlxGa1-x)2O3
β-Ga2O3
5 nm

Figure 8

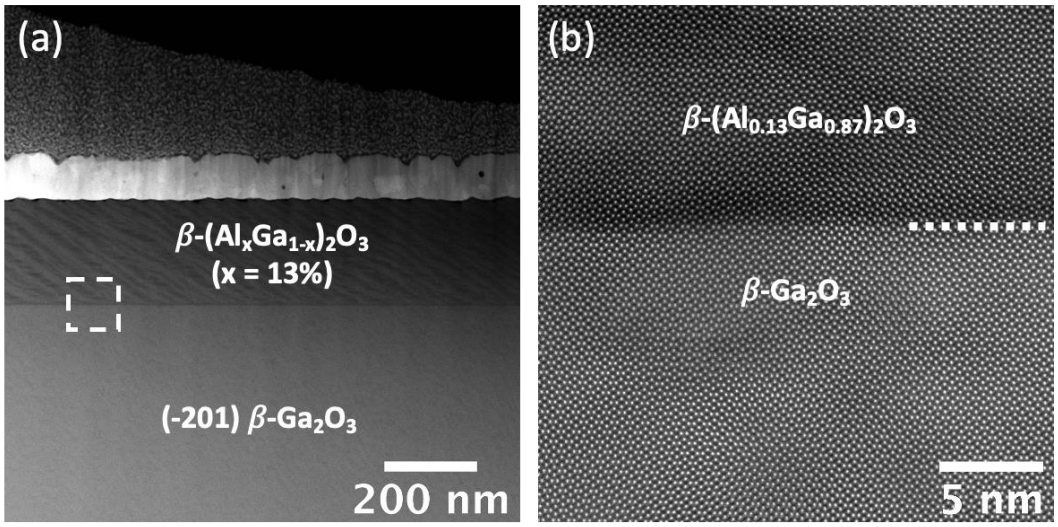
(a)
β-(AlxGa1-x)2O3
(x = 13%)
(-201) β-Ga2O3
200 nm
(b)
β-(Al0.13Ga0.87)2O3
β-Ga2O3
5 nm

Figure 9

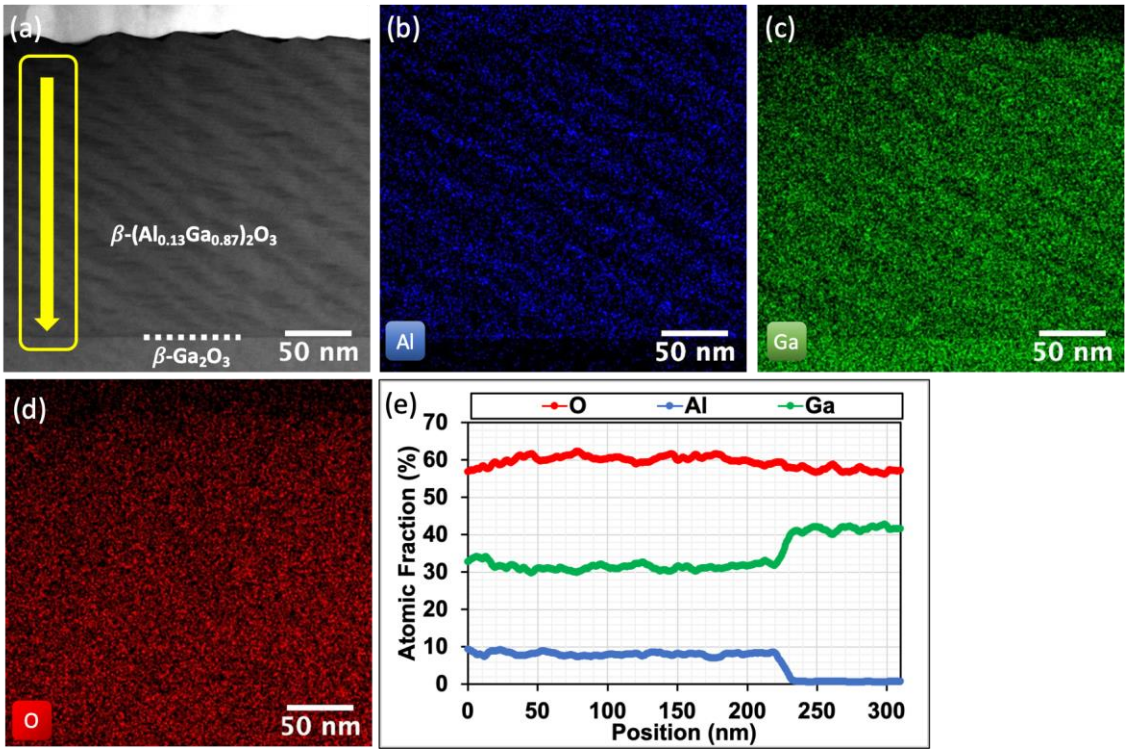
(a)
β-(Al0.13Ga0.87)2O3
β-Ga2O3
50 nm
(b)
Al
50 nm
(c)
Ga
50 nm
(d)
O
50 nm
(e)
O
Al
Ga
Atomic Fraction (%)
Position (nm)
0
10
20
30
40
50
60
70
0
50
100
150
200
250
300

Figure 10

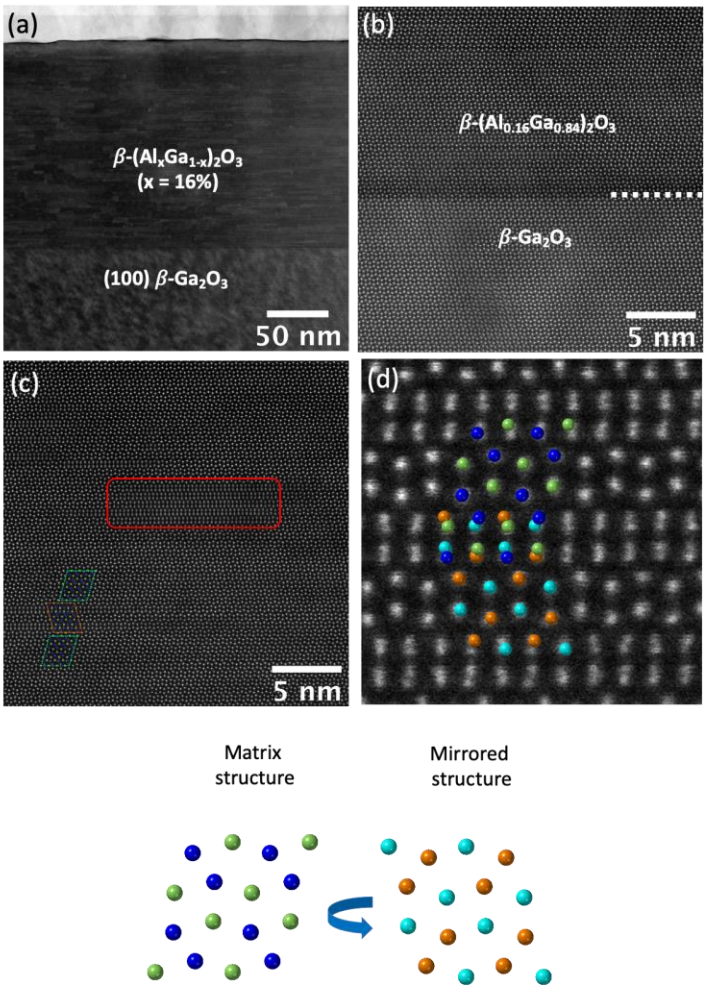
(a)
β-$(Al_xGa_{1-x})_2O_3$
(x = 16%)
(100) β-Ga_2O_3
50 nm
(b)
β-$(Al_{0.16}Ga_{0.84})_2O_3$
β-Ga_2O_3
5 nm
(c)
5 nm
(d)
Matrix
structure
Mirrored
structure

Figure 11

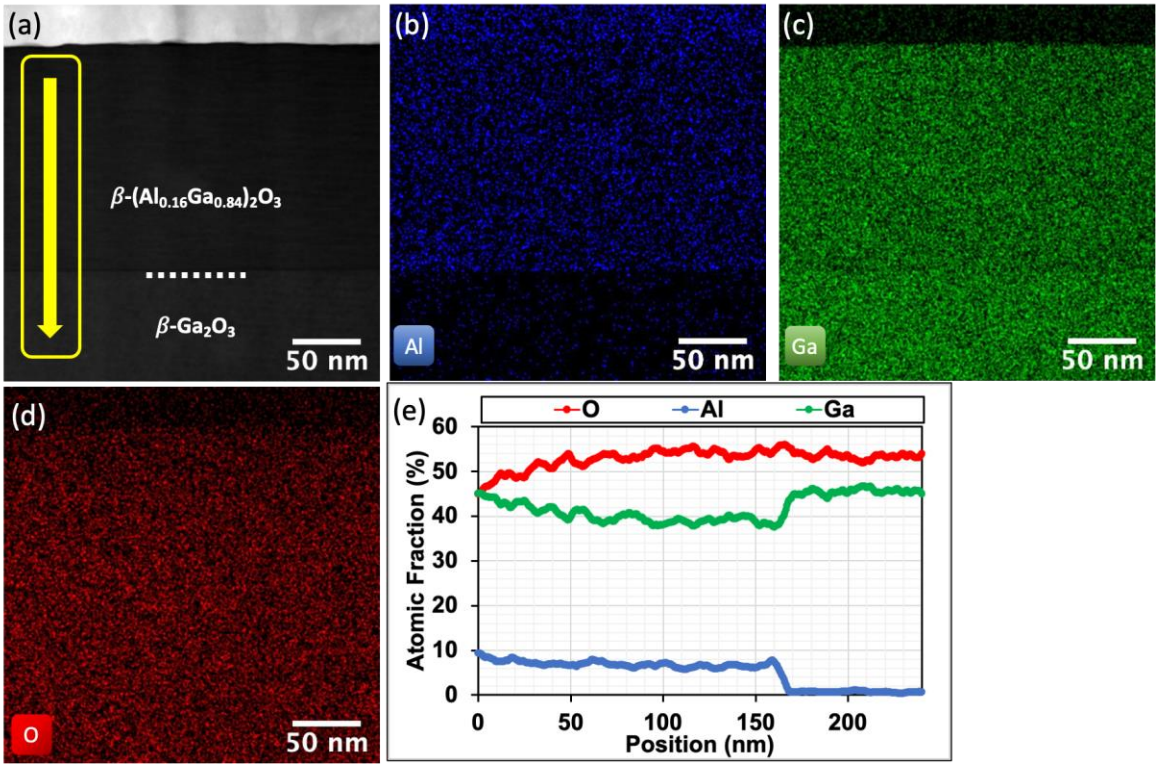
(a)
β-$(Al_{0.16}Ga_{0.84})_2O_3$
β-Ga_2O_3
50 nm
(b)
Al
50 nm
(c)
Ga
50 nm
(d)
O
50 nm
(e)
O
Al
Ga
Atomic Fraction (%)
0
10
20
30
40
50
60
0
50
100
150
200
Position (nm)

Figure 12

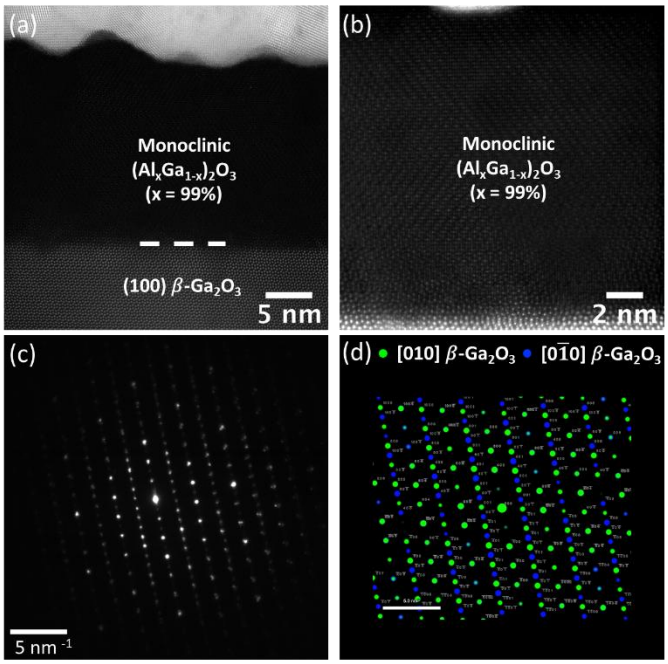
(a)
Monoclinic
$(Al_xGa_{1-x})_2O_3$
(x = 99%)
(100) β-Ga_2O_3
5 nm
(b)
Monoclinic
$(Al_xGa_{1-x})_2O_3$
(x = 99%)
2 nm
(c)
5 nm^{-1}
(d)
[010] β-Ga_2O_3
[0$\bar{1}$0] β-Ga_2O_3

Figure 13

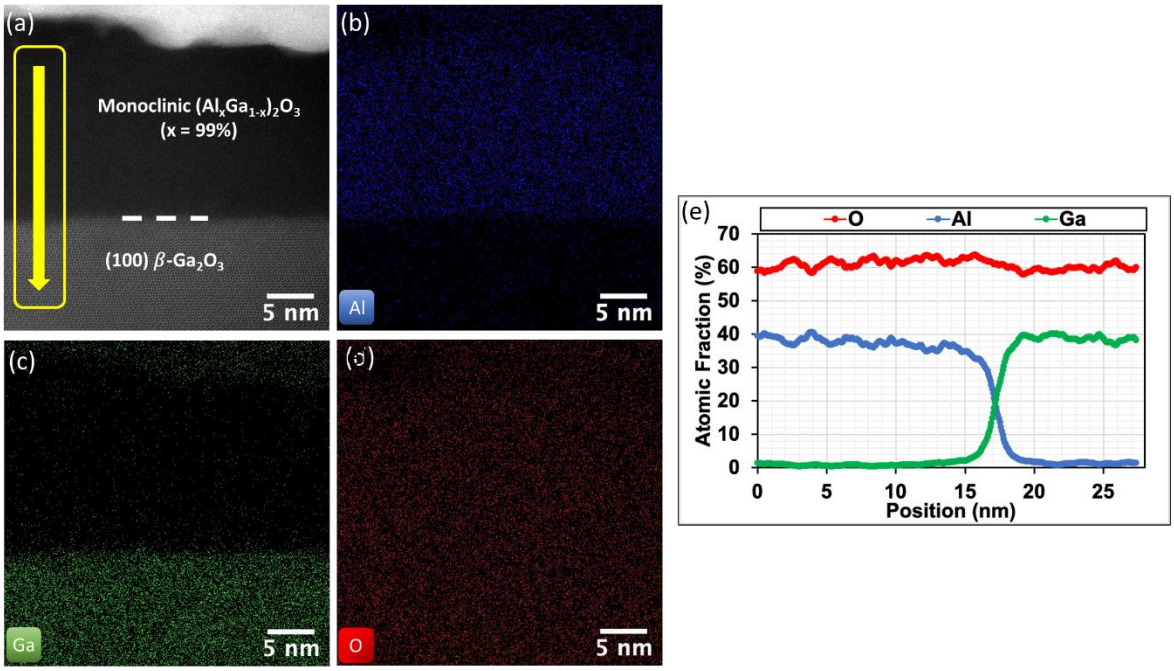
(a)
Monoclinic $(Al_xGa_{1-x})_2O_3$
(x = 99%)
(100) β-Ga_2O_3
5 nm
(b)
Al
5 nm
(c)
Ga
5 nm
(d)
O
5 nm
(e)
O
Al
Ga
Atomic Fraction (%)
70
60
50
40
30
20
10
0
0
5
10
15
20
25
Position (nm)

Figure 14

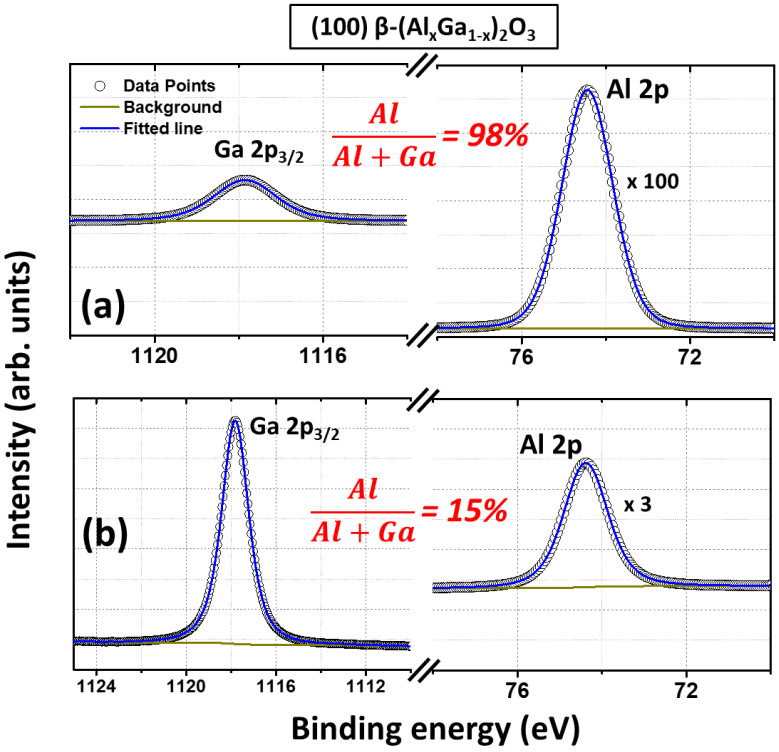
(100) β-(Al$_x$Ga$_{1-x}$)$_2$O$_3$
Data Points
Background
Fitted line
Ga 2p$_{3/2}$
$\frac{Al}{Al+Ga}$ = 98%
Al 2p
x 100
(a)
1120
1116
76
72
Ga 2p$_{3/2}$
$\frac{Al}{Al+Ga}$ = 15%
Al 2p
x 3
(b)
1124
1120
1116
1112
76
72
Intensity (arb. units)
Binding energy (eV)

Figure 15

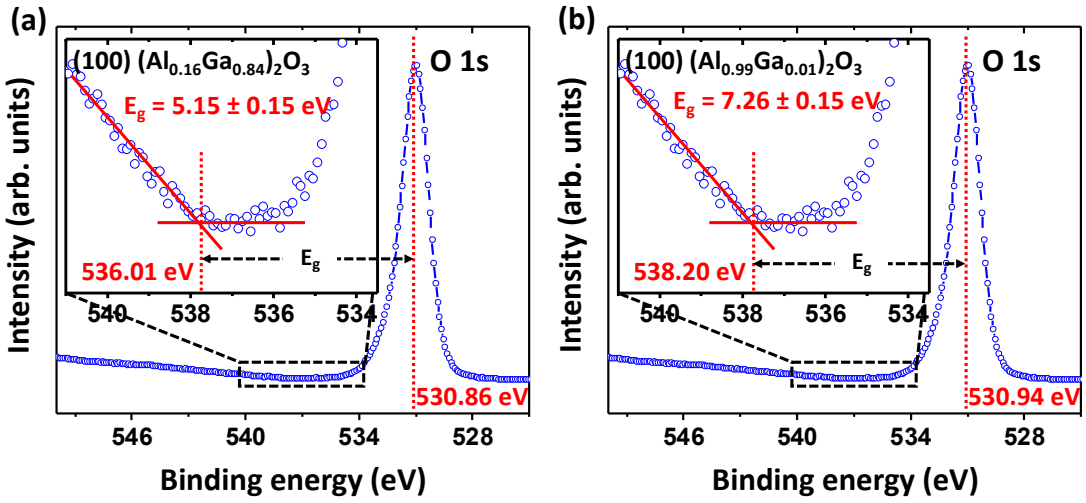
(a)
(100) (Al0.16Ga0.84)2O3
Eg = 5.15 ± 0.15 eV
O 1s
536.01 eV
Eg
530.86 eV
Intensity (arb. units)
Binding energy (eV)
(b)
(100) (Al0.99Ga0.01)2O3
Eg = 7.26 ± 0.15 eV
O 1s
538.20 eV
Eg
530.94 eV
Intensity (arb. units)
Binding energy (eV)

Figure 16

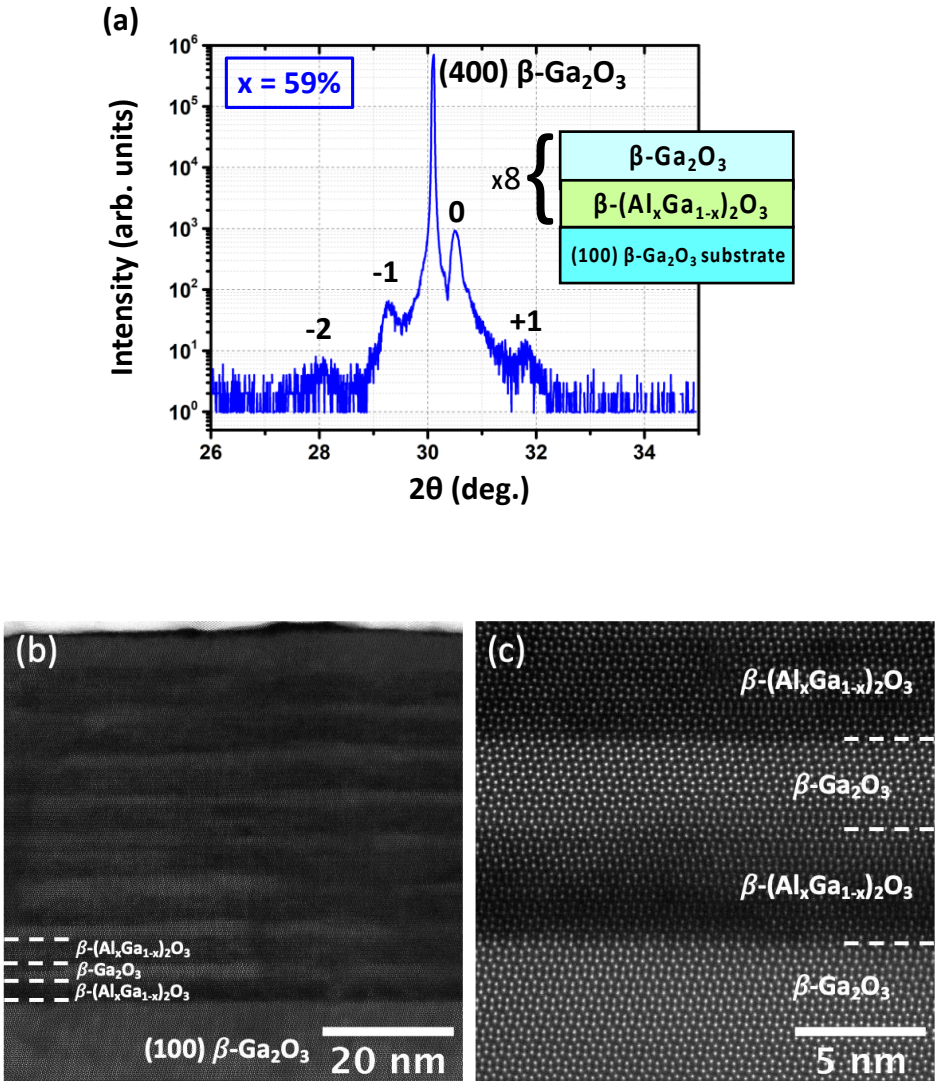
(a)
x = 59%
(400) β-Ga2O3
x8
β-Ga2O3
β-(AlxGa1-x)2O3
(100) β-Ga2O3 substrate
0
-1
-2
+1
Intensity (arb. units)
2θ (deg.)
(b)
β-(AlxGa1-x)2O3
β-Ga2O3
β-(AlxGa1-x)2O3
(100) β-Ga2O3
20 nm
(c)
β-(AlxGa1-x)2O3
β-Ga2O3
β-(AlxGa1-x)2O3
β-Ga2O3
5 nm

Figure 17

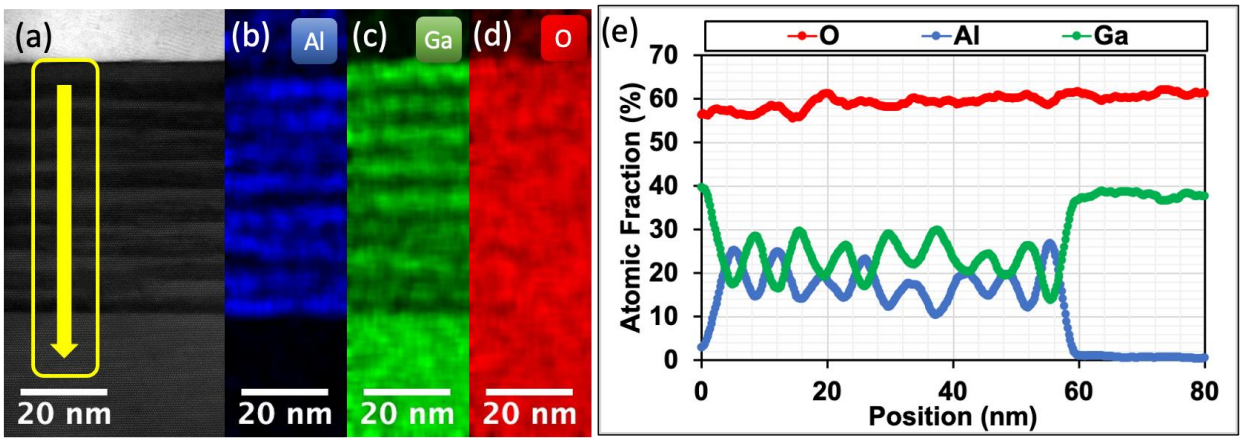
(a)
(b)
Al
(c)
Ga
(d)
O
20 nm
20 nm
20 nm
20 nm
(e)
O
Al
Ga
Atomic Fraction (%)
70
60
50
40
30
20
10
0
0
20
40
60
80
Position (nm)